REVIEW

Check for updates

Constructing a high-performance bifunctional MnO₂-based electrocatalyst towards applications in rechargeable zinc–air batteries

Xiufeng Yi, [a] Yijian Song,[a] Duzheng He,[a] Weijie Li,[b] Anqiang Pan[ac] and Chao Han [*a]

Slow oxygen reduction reaction (ORR) and oxygen evolution reaction (OER) at the liquid–solid–gas interface of the air cathode have always been a big obstacle for different renewable energy devices, especially rechargeable zinc–air batteries (RZABs). In recent years, manganese dioxide based electrocatalysts have been extensively investigated for their variety of morphologies and structures, relatively high activity, rich resources and environmental friendliness. Not only that, manganese dioxide based electrocatalysts can be used as cathode materials for zinc ion batteries, which is conducive to the development of zinc–air ion batteries. This review serves to summarize the latest research progress on manganese dioxide as a high-performance bifunctional (both OER and ORR) catalyst for zinc–air batteries. Although MnO₂ has many advantages and has been studied extensively, its activity and stability still need to be improved. This review aims to guide the design and widespread application of Mn-based electrocatalysts in the future by summarizing various measures to enhance performance.

1 Introduction

In the rapidly developing modern society, the acceleration of industrialization and rapid urbanization have led to an unprecedented growth in demand for energy. However, the rapid growth in energy demand has created a serious problem-the depletion of fossil fuels. At the same time, the overuse of fossil fuels has led to growing environmental problems.[1–3] To achieve the goal of a green economy and mitigate the burden of environmental pollution, the search for high-efficiency, clean and long-lasting substitutes to fossil energy has become a critical step to be taken without delay.[4–7] Sustainable energy resources, including solar, wind and tidal power, have grown rapidly, but the cost of storing and converting them has remained high over the last several years.[8–10] In comparison, metal–air batteries such as zinc–air batteries (ZABs), as a new type of energy transformation and storage device, are gradually receiving widespread attention in industry, and are regarded as one of the important development directions for future energy technologies.[11–13] These devices are suitable for responding to the fast-growing demands in mobile communication, emergency storage, electric vehicles, and mass energy storage due to their cost-effectiveness, high specific energy and stable discharge voltage.[14–16] In particular, zinc–air batteries possess the advantages of high safety, high theoretical specific energy density (1218 W h kg⁻¹), promising volumetric energy density of 6136 W h L⁻¹, low cost, abundance of the constituent elements and environmental friendliness.[17–19] Moreover, non-rechargeable ZABs have already been commercialized, offering an excellent industrial fundament for rechargeable zinc–air batteries (RZABs). Therefore, they have been regarded as one of the most promising metal–air batteries for future energy storage techniques.[20–22]

Nevertheless, the reversible oxygen reaction is a multistep complex process that involves not only the transfer of electrons but is also closely related to the coupling of protons. Specifically, the oxygen needs to experience a series of intermediate state changes, which are accompanied by the exchange of electrons and protons during the ORR and OER process at the air-cathode. These multi-step and proton-coupled electron transfer processes result in slow rates of reaction kinetics. This means that during the battery charging and discharging process, the oxygen conversion efficiency is not high, thus limiting the overall performance of the battery. In general, this slow kinetic rate not only affects the charging and discharging speed of the battery but may also lead to performance degradation and shortened life of the battery during long-term use, which strongly hinders the widespread popularization and applications of rechargeable zinc–air batteries.[23,24] One possible

a School of Materials Science and Technology, Central South University, Changsha 410083, Hunan Province, P. R. China

b Powder Metallurgy Research Institute, Central South University, Changsha 410083, Hunan Province, P. R. China

c Xinjiang Engineering Research Center of Environmental and Functional Materials, School of Materials Science and Engineering, Xinjiang University, Urumqi, Xinjiang 830046, P. R. China
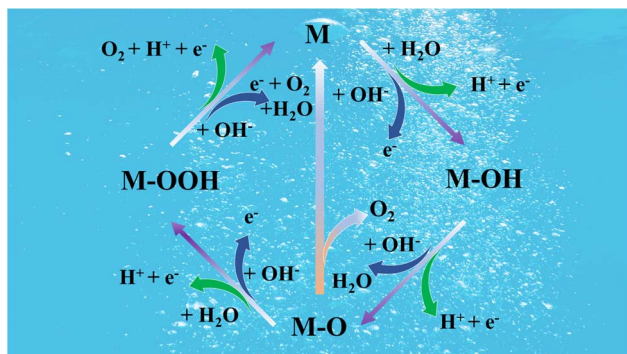
This journal is © The Royal Society of Chemistry 2024

J. Mater. Chem. A, 2024, 12, 29355–29382 | **29355**

Fig. 1   The reaction pathway of the ORR and OER.

response pathway for the ORR/OER mechanism is shown in Fig. 1.

The "M" represents the active site that adsorbs reactants, intermediates, and products. The intermediates in the adsorption process are represented by M–OH, M–O, and M–OOH. Therefore, to improve the performance of RZABs, it is essential to develop high-performance ORR and OER catalysts.[25–27] Although noble metal based catalysts (Pt and Ru/Ir) are considered the most outstanding catalysts for the ORR and OER,[22,28,29] the drawbacks of scarcity of their natural resources, poor durability and the inability of a single precious metal to have excellent bifunctional properties at the same time have severely limited the large-scale production and application of zinc–air batteries.[30–33] In particular, the synthesis of highly economical and highly efficient bi-functional non-noble metal based electrocatalysts, such as carbon-based materials, transition metal compounds and their composites, for the ORR and OER is greatly significant for the widespread adoption of zinc–air batteries.[34–36]

The processes of ORR and OER usually share the same oxygen intermediates and the real reaction mechanism is complex. During the reaction, disparate oxygenated intermediates are sequentially adsorbed onto the active site. The likelihood of each step in the reaction largely hinges on the adsorption energy of the relevant oxygen-bearing species. If the interaction between the active site and the oxygen-bearing species is excessively strong, desorption of the product becomes challenging. Conversely, if the adsorption of the oxygen-containing group by the active part is not sufficiently strong, the reaction is difficult to proceed.[37] Therefore, excellent ORR/OER electrocatalysts should have moderate adsorption energy for oxygen-containing intermediates (M–O, M–OH, M–OOH).[38] The ORR and OER performance of the catalyst is strongly associated with the adsorption energy of the oxygen-containing intermediates. The adsorption energies of M–OH and M–OOH intermediates exhibit an inherent linear scaling relationship.[39] No catalyst can perform the ORR and OER without an overpotential due to the effects of scaling relationships. When the adsorption energy of one intermediate is changed, the adsorption energy of the other intermediate changes accordingly, and therefore a catalyst with a single active site cannot concurrently achieve optimal ORR and OER

activity.[40] Therefore, to enhance the OER and ORR individually or together, the scaling relationship must be overcome. For example, to break the limitations of the linear scaling relation, Zhou et al. proposed a fast four-electron two-site reaction mechanism in which a suitable atomic distance between two neighboring metal active sites can inhibit the production of M–OOH, breaking O–O radicals (M–O–O–M), and limit the selectivity of the two-electron reaction path in the ORR process.[41] Not only that, alkali metals serve as a crucial factor in tuning the lattice oxygen reactivity and scaling relationships.[42] In conclusion, bifunctional performance can be efficiently realized by appropriately adjusting the geometry, electronic configuration and the surrounding chemical environment of the active site, or by mixing monofunctional ORR and OER electrocatalysts.

In addition to the slow cathodic reaction, the alkaline electrolyte causes passivation of the zinc anode and dendrite growth, both of which can hinder the commercialisation of rechargeable zinc–air batteries. Zinc reacts with OH^- on the electrode surface to form an insulating ZnO passivation film, which reduces the utilisation of the zinc anode and results in the actual energy density of zinc–air batteries lagging far behind the theoretical value.[11] The formation of zinc dendrites is mainly due to uneven deposition of Zn and uneven distribution of $Zn(OH)_4^{2-}$ on the zinc anode surface.[43] Further growth of Zn dendrites can puncture the cell diaphragm and cause internal short circuits, shortening the cycle life of Zn-based batteries and limiting their practical applications.[44] Controlling the formation of zinc dendrites is essential to extend the cycle life of zinc–air batteries.

Among all the possible non-noble bifunctional catalysts, manganese dioxide has attracted much attention, owing to its unbeatable merits, such as multiple valence states, diverse morphology and structure, low cost, rich resources, environmental friendliness and excellent catalytic activity as seen in Fig. 2.[33,45–48] In addition, manganese dioxide is more commonly commercialized, not only as a cathode material for zinc ion batteries and supercapacitors but can also contribute to the development of zinc–air batteries.[49,50] Not only that, during the electrochemical reaction, the passivation film on the manganese dioxide surface can hinder direct contact of the cathode with the electrolyte to avoid further decomposition of the electrolyte.[51] MnO_2 helps to maintain the chemical balance of the electrolyte and reduce the occurrence of side reactions during the reaction process. A stable electrolyte environment is essential to inhibit the formation of zinc dendrites. Importantly, MnO_2 can provide uniform active sites on the electrode surface and disperse the current density. This uniform current distribution effectively reduces the formation of localised areas of high current density and reduces the rapid deposition rate of zinc ions in specific areas, thereby inhibiting the growth of zinc dendrites. However, there are few reviews of manganese dioxide based electrocatalyst applications in zinc–air batteries. It has not been reported that different strategies are used to improve the electrocatalytic ability of manganese dioxide-based cathodes in zinc–air batteries. Hence, as demonstrated in Fig. 2, we focus more on the latest research progress on manganese dioxide as a superior catalyst for zinc–air batteries in the field of
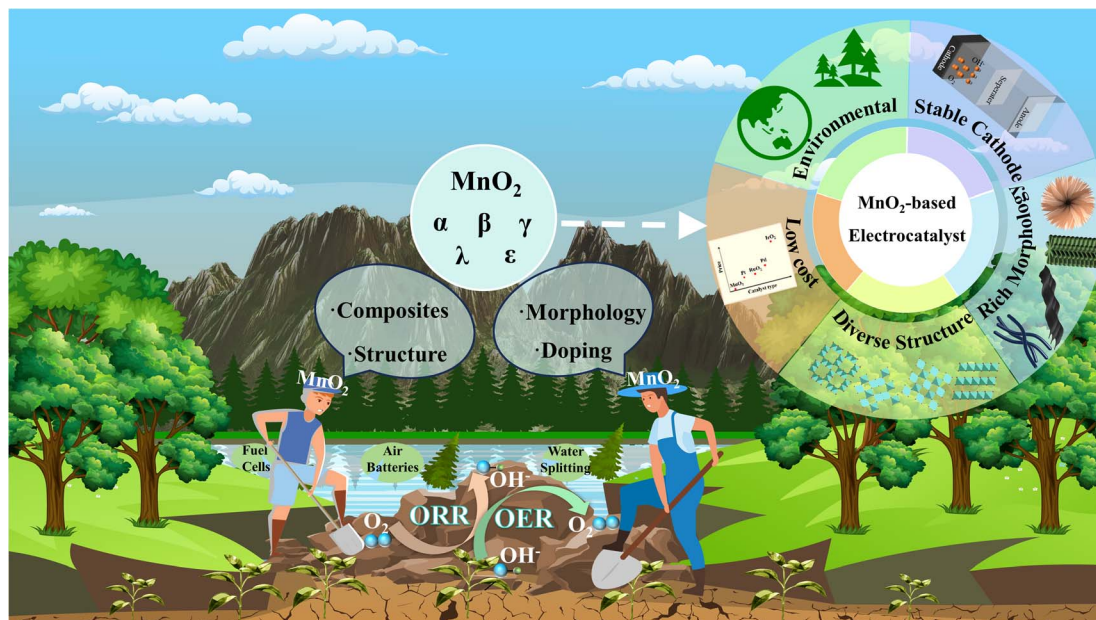
Fig. 2 Advantages of the MnO$_2$ catalyst and four different strategies towards constructing a bi-functional MnO$_2$ catalyst.

improving the OER/ORR electrocatalytic activity of manganese dioxide by structural and morphological control, doping engineering, and composite material formation.

2 Recent progress on manganese dioxide electrocatalysts

Like for other electrocatalysts,[52,53] the general approach for realizing and enhancing the catalytic performance of MnO$_2$ is to improve its conductivity, increase the count of active sites and enhance its inherent activity. Moreover, specific ideas are also needed to further improve the OER/ORR performance of MnO$_2$. Based on the above information, four practical approaches including controlling the morphology and crystal structure, doping of heteroatoms and formation of composites are summarized and will be discussed in the following part.

2.1 Control of crystal structure

It is found that the electrocatalytic properties of manganese dioxide are mainly influenced by the crystal structure of manganese dioxide.[35,54] Manganese dioxide consists of the MnO$_6$ octahedral structural unit, in which the manganese atom occupies the center of the octahedron, while the oxygen atom is situated at the apex of its corners.[4] Depending on how their structural units are combined, they can be divided into three types, namely one-dimensional tunneling structures (α-, β-, γ- and ε-MnO$_2$), two-dimensional laminar structures (δ-MnO$_2$) and three-dimensional structures (λ-MnO$_2$).[55] α-MnO$_2$ is formed by double chains formed by the octahedra of MnO$_6$ extending infinitely along the c-axis through co-angles with (1×1) and (2×2) tunneling structures. The (2×2) tunneling system in α-MnO$_2$ can accommodate most metal cations (*e.g.*, K$^+$, Ca^{2+}, Na$^+$, Mg^{2+}, Pb^{2+} *etc.*) and water molecules, making it suitable as an

adsorbent and catalytic material.[53] δ-MnO$_2$ consists of MnO$_6$ octahedra connected by coprime and extending infinitely along the "*ab*" axis, with a two-dimensional layered structure. Compared to other MnO$_2$ crystalline forms, δ-MnO$_2$ has the largest pore space and a high specific capacity when used as an electrode material due to its large interlayer space ($\sim$7 Å) and tunnel size ($\sim$4.6 Å).[56] β-MnO$_2$ is considered to be the most stable structure, but it is not suitable as a catalytic material, owing to the lowest surface area, pore volume, low discharge capacity and narrow tunneling, which usually only accommodates small ions such as H$^+$ or Li$^+$. It is well known that the ORR pathway exhibits a pronounced sensitivity to structural factors, significantly influenced by the surface geometry, electronic configuration, and sites for O$_2$ adsorption.[57] Therefore, it is documented that the ORR activity of MnO$_2$ increases in the following order: β-MnO$_2$ < λ-MnO$_2$ < γ-MnO$_2$ < α-MnO$_2 \approx \delta$-MnO$_2$ in alkaline medium. However, the OER activity exhibits a sequential trend in alkaline media, with δ-MnO$_2$ demonstrating the lowest activity, followed by β-MnO$_2$, then amorphous manganese dioxide (AMO), and ultimately α-MnO$_2$ displaying the highest activity.[58] It is easy to conclude that α-MnO$_2$ is an excellent catalyst towards both the OER and ORR. Therefore, manipulating the crystal forms is an effective means of constructing a bifunctional MnO$_2$ catalyst.

2.1.1 ORR performance. Yang *et al.* successfully prepared one-dimensional structures including nanowires and nanorods with different crystalline phases (α-MnO$_2$ and β-MnO$_2$) by a simple hydrothermal process (Fig. 3a).[59] The α-MnO$_2$ with (2×2) tunneling structure can allow more molecules, ions, and electrons to pass through, resulting in more oxygen molecules bonding with electrons. In addition, the specific surface area of α-MnO$_2$ nanowires is a key factor for their excellent performance. Due to the nanoscale size, α-MnO$_2$ nanowires have an extremely high specific

This journal is © The Royal Society of Chemistry 2024

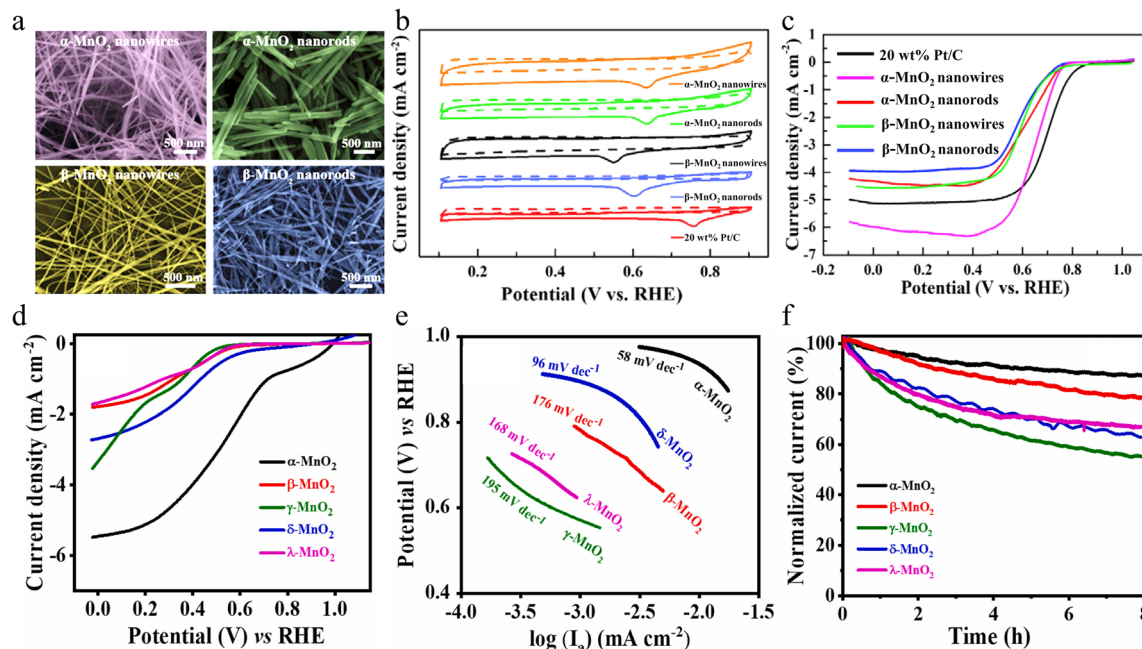*J. Mater. Chem. A*, 2024, **12**, 29355–29382 | **29357**

Fig. 3 The ORR performance and surface morphology of different MnO_2. (a) SEM images of the samples obtained. (b) CV curves and (c) LSV curves of the obtained MnO_2 and 20 wt% Pt/C. Reproduced with permission.[59] Copyright 2019, Elsevier. (d) LSV curves, (e) Tafel slope and (f) chronoamperograms of MnO_2 with different crystal structures. Reproduced with permission.[60] Copyright 2023, Elsevier.

surface area, and more active sites can be provided at the interface of the three phases throughout the ORR process, thus enhancing the ORR electrocatalytic efficiency. As described in Fig. 3b and c, α-MnO_2 nanowires display better cathode peaks than other structures of MnO_2, and the diffusion limited current density is higher. The methodology used in this study is simple and the study provides a clear link between the structure of the material and its catalytic properties, showing that the key determinants of catalytic activity are closely linked to the stacking pattern within the MnO_2. However, the effect of the crystal structure on its catalytic performance can be further determined by comparing the ORR performance of more MnO_2 crystalline phases. In addition, the long-term stability of the material under operating conditions could be further explored.

Subramaniam *et al.* prepared five different crystalline forms of manganese dioxide with similar structural features using a hydrothermal method and further investigated the ORR catalytic properties of manganese dioxide with different crystalline phases.[60] Electrochemical studies have shown that α-MnO_2 exhibits the best ORR catalytic performance, such as the largest limiting current density and the lowest Tafel slope value as well as 88.2% current retention after an 8 hour test (Fig. 3d–f). This is attributed to the fact that α-MnO_2 has larger and more stable tunnels/interlayer spaces and a higher proportion of surface oxygen functional groups, which offer more active adsorption sites and promote electron transfer, thus making it superior to other crystal structures of MnO_2 in the ORR. This study provides a detailed understanding of how crystal structure affects catalytic activity. Moreover, a simple hydrothermal method allows the synthesis of controllable crystal phases of MnO_2 to enhance ORR activity, which lays the foundation for

the development of more efficient catalysts for energy conversion and storage applications.

2.1.2 OER performance. Subramaniam *et al.* simultaneously compared the catalytic oxidation activity of five different crystal structure MnO_2 catalysts for OH^-, and found that the crystal structure has a great impact.[60] It is shown that α-MnO_2 and δ-MnO_2 have higher onset potentials, lower Tafel slopes and smaller charge transfer resistance (R_{ct}) (Fig. 4a–c). The electrode potential of α-MnO_2 exhibits excellent stability over time at the current density of 10 mA cm^{-2}, with the potential value remaining almost constant as shown in Fig. 4d. However, the δ-MnO_2 electrode potential exhibits an upward trend in the initial stage and is not suitable for long-term studies. During the reaction of δ-MnO_2, if oxygen continues to escape from its surface, this process may disrupt the stable layered structure of K^+ and H_3O^+ ions, resulting in poor stability. The design of the widened tunnel, large layer distance and low R_{ct} value effectively improved the wetting properties of α- and δ-MnO_2, which is conducive to the adsorption of hydroxyl ions and then the OER activity is increased. The relationship between the crystal structure and the electrochemical properties of the OER has been thoroughly investigated by various characterisation and analysis methods. This contributes to a better understanding of how to optimize the OER performance of MnO_2, leading to the development of more efficient electrocatalysts.

The electrocatalytic OER activity can also be enhanced by modulating the electron distribution of the electrocatalytic active site by stabilizing the metastable state of the electrocatalyst or by non-natural polymorphs. Gupta and colleagues synthesized different polycrystalline types (β/N (native)-MnO_2,

29358 | *J. Mater. Chem. A*, 2024, **12**, 29355–29382

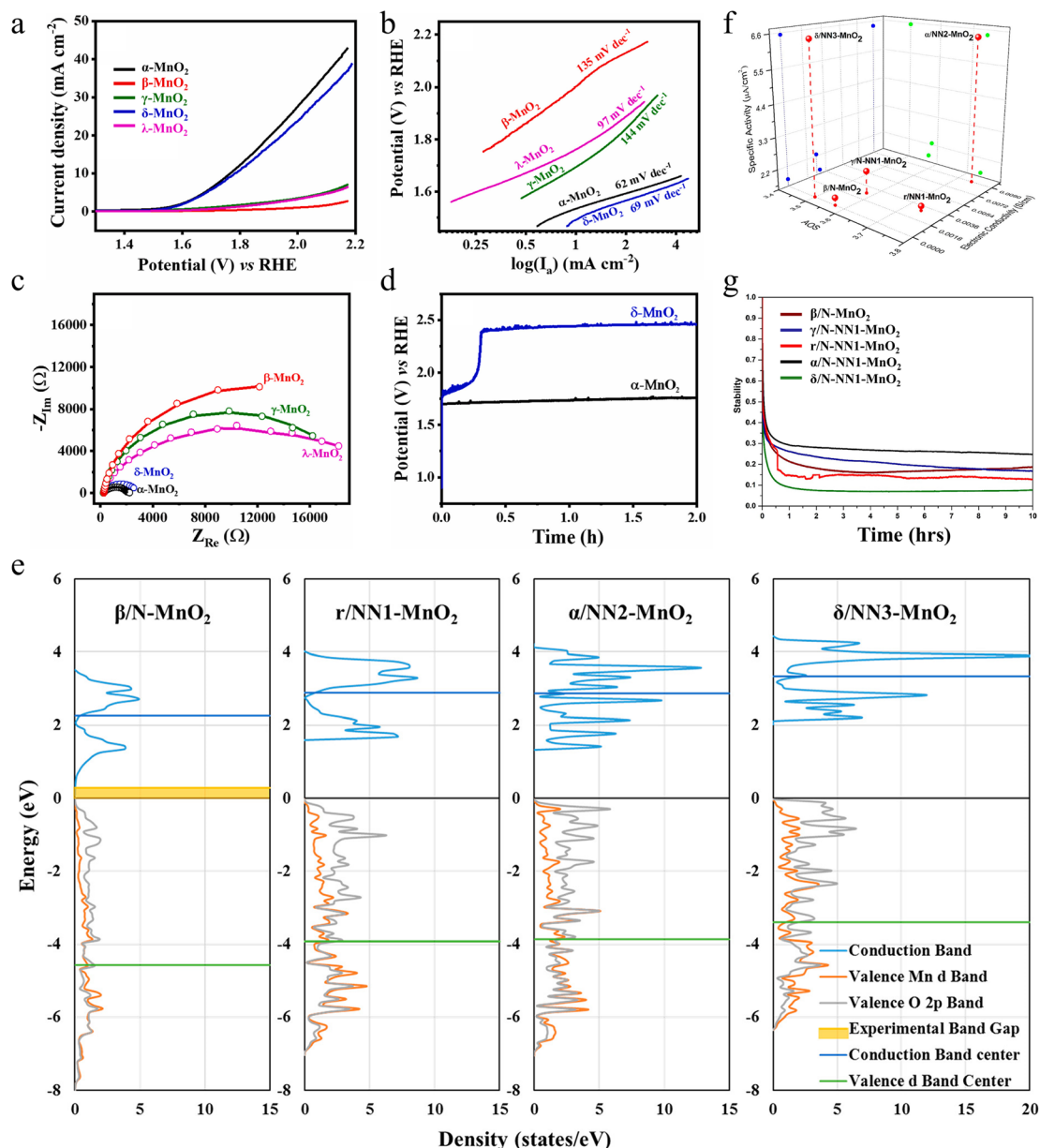This journal is © The Royal Society of Chemistry 2024

Fig. 4 The OER performance of different monocrystalline and polymorphs of MnO$_2$. (a) LSV curves, (b) Tafel slopes, (c) EIS spectra and (d) chronopotentiogram of MnO$_2$ with different crystal structures. Reproduced with permission.[60] Copyright 2023, Elsevier. (e) Density of states plot. (f) Specific OER activities of different polymorphs of MnO$_2$ with their oxidation state of Mn (AOS) and bulk electronic conductivities. (g) Stability analysis. Reproduced with permission.[61] Copyright 2019, American Chemical Society.

γ/N (native)-NN1 (non-native)-MnO$_2$, α/NN2 (non-native)-MnO$_2$ and δ/NN3 (non-native)-MnO$_2$) through the hydrothermal technique and γ/NN1 (non-native)-MnO$_2$ by a slow acidification reaction.[61] It is widely acknowledged that the adsorption coverage of oxygen and adsorption strength on the MnO$_2$ surface has a crucial impact on the OER activity. The higher the Mn-d valence band, the less the antibonding states are occupied and the stronger the O adsorption. The upward shift of the central position of the Mn-d valence band of δ/NN3-MnO$_2$ and α/NN2-MnO$_2$ approaching the Fermi energy level enhances the adsorption of oxygen, which decreases the activation barriers of

the OER (Fig. 4e). The low surface oxidation state of Mn (such as the appearance of Mn^{3+}) in the polycrystalline structure and the higher electronic conductivity of the material can also provide higher OER activity. This is the case for δ/NN3-MnO$_2$, which exhibits the lowest Mn oxidation state (AOS) among MnO$_2$ polymorphs (Fig. 4f). Due to the unique non-native properties of α/NN2-MnO$_2$, oxygen vacancies are more likely to form in α/NN2-MnO$_2$, leading to higher electronic conductivity. However, when polycrystalline forms undergo surface reconstruction, they undergo major dissolution during the first-hour test under the action of electrochemical potential, which leads to

a decrease in activity (Fig. 4g). This study particularly highlights the importance of stability of the non-native structure, which has the potential to significantly improve the electrocatalytic activity, providing more options and research directions for the development of more efficient electrocatalysts for the OER. By deeply analysing and deconstructing the relationship between oxidation state, conductivity, and specific activity among MnO_2 polycrystals, the research results not only contribute to a deeper understanding of the electrocatalytic properties of MnO_2 but also have a wide applicability that can be extended to other electrocatalytic material systems.

2.1.3 ORR & OER performance in a zinc–air battery. It can be observed that new types of improved ORR or OER electrocatalysts can be obtained by reasonable structural engineering design. The crystal structure–characteristics relationships of MnO_2 indicate that α-MnO_2 exhibits superior activity in both the ORR and OER in comparison to the others. Gu *et al.* prepared ultrathin α-MnO_2 nanowires with high crystallinity for bifunctional oxygen catalysts based on an ionic liquid (IL)-assisted hydrothermal method.[62] The crystalline structure and morphology of the reaction products were changed from β-MnO_2 nanorods (MnO_2-IL_0) to α-MnO_2 nanowires (MnO_2-$IL_{0.5}$)

by increasing the amount of IL, and the crystallinity of α-MnO_2 nanowires was further improved by extending preparation time. The α-MnO_2 nanowire shows excellent bifunctional performance due to its large K^+ embedded tunneling structure, high Mn^{3+} quantities and oxygen-rich vacancies, as well as its ultra-thin nanowire morphology with high surface area. Because of these, the activation energy of the reaction is reduced and the reaction rate is accelerated, leading to more efficient energy conversion and storage. As a result, the MnO_2-IL0.5 sample reaches a larger half-wave potential ($E_{1/2}$) of 0.83 V (Fig. 5a), which is slightly lower than that of the Pt/C (0.85 V). In particular, Fig. 5b shows the favorable OER performance of the MnO_2-$IL_{0.5}$ electrode; it demonstrates 394 mV minimal overpotential at the current density of 10 mA cm^{-2}, just a 104 mV increase compared to the overpotential of the benchmark RuO_2 catalyst. When MnO_2-$IL_{0.5}$ is used as an electrocatalyst on the air cathode of the zinc–air battery, the battery displays outstanding performance, including excellent electrochemical stability for 40 hours at the current density of 10 mA cm^{-2} as shown in Fig. 5c. The electrocatalyst is synthesized using a very simple method, which not only has the advantages of high operability and low cost but is also easy to be produced on a large scale. These
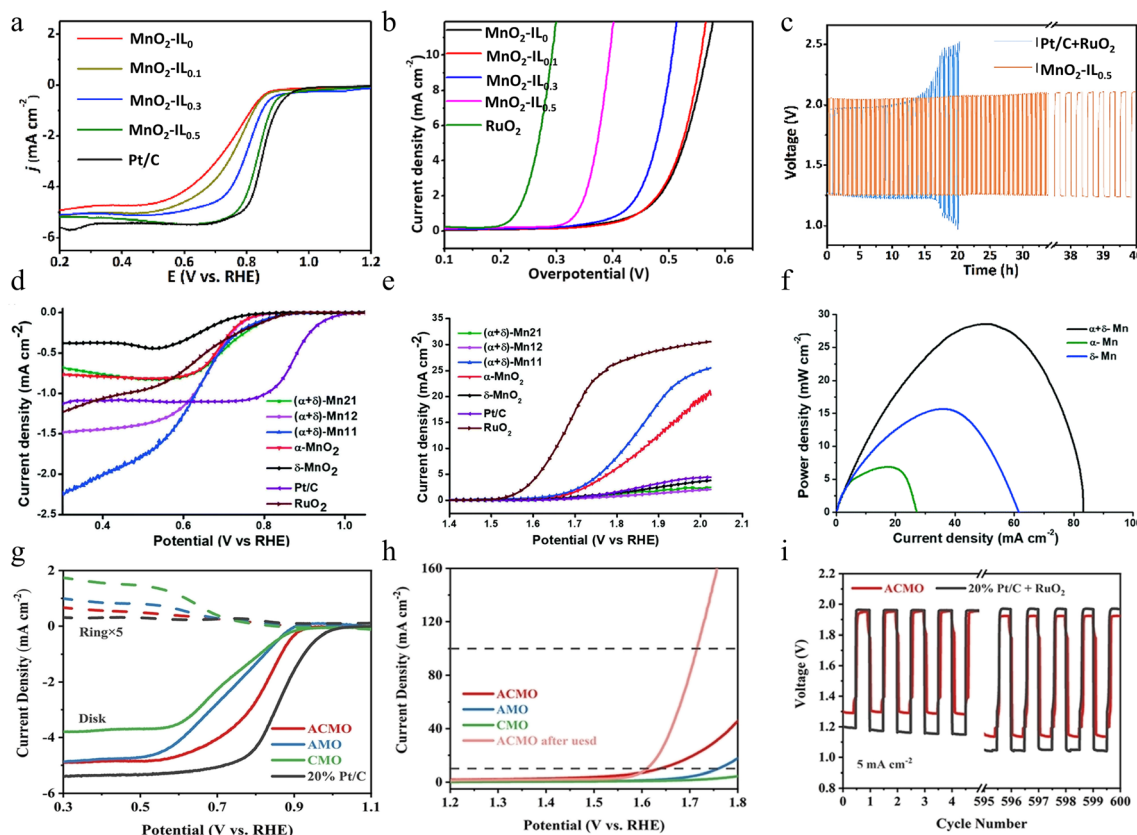

Fig. 5 The electrocatalytic performance of manganese dioxide with different structures. (a) ORR polarization curves and (b) OER polarization curves of various MnO_2-IL samples prepared by an ionic liquid (IL)-assisted hydrothermal method at a scan rate of 5 mV s^{-1}. (c) Stability comparison between Pt/C + RuO_2 and MnO_2-$IL_{0.5}$ electrodes at 10 mA cm^{-2}. Reproduced with permission.[62] Copyright 2019, Elsevier. (d) ORR polarization curves, (e) OER polarization curves, and (f) corresponding power density curves of ($\alpha+\delta$)-MnO_2 composites prepared by a grinding and annealing method. Reproduced with permission.[63] Copyright 2020, Royal Society of Chemistry. (g) LSV curves for the ORR, (h) LSV curves for the OER, and (i) charge–discharge curves of ACMO prepared by the oxidation method. Reproduced with permission.[64] Copyright 2022, Wiley-VCH.

29360 | *J. Mater. Chem. A*, 2024, **12**, 29355–29382

This journal is © The Royal Society of Chemistry 2024

batteries can provide a stable power supply for LED displays, showing excellent practical application results. These batteries show great promise for energy storage devices in portable electronics and are expected to be widely used in smart devices, wearable technology and other portable electronic devices in the future.

Although single-phase MnO_2 has been well explored as a catalytic material, it suffers from the disadvantages of low stability, low conductivity, and small ion diffusion constants. Synthesizing catalyst materials containing two different manganese dioxide structures with synergistic effects is a useful way to achieve multiple catalytic effects. Mathur and colleagues developed a composite material comprising α- and δ-MnO_2 through a combination of grinding and annealing techniques.[63] Tunneling structure enables the prepared composites to better cope with high current density and fast charge/discharge during the electrochemical storage process. Specifically, the layered structure results in the formation of many tiny, laminated voids and channels within the composite material. These voids and channels not only increase the overall surface area of the material but also provide more paths and opportunities for electrolyte ions to penetrate the interior of the material more easily. More importantly, the layered structure also increases the number of active sites in the composite. This unique structural combination brings multiple positive effects to the composite material. As a result, both the capacity and the charge/discharge efficiency of the battery are significantly enhanced. This enhancement not only allows the battery to store more energy but also makes the battery more stable and reliable during the charging and discharging process, thus extending the service life of the battery. As shown in Fig. 5d, the $(\alpha+\delta)$-MnO_2 composites exhibit more favorable onset potentials compared to pure MnO_2 materials, close to that of commercial RuO_2. $(\alpha+\delta)$-Mn11 (which contains equal amounts of α- and δ-MnO_2) shows a smaller overpotential (Fig. 5e) in the OER. In addition, $(\alpha+\delta)$-Mn11 exhibits better bifunctional properties than α-MnO_2. The application of the prepared composite materials in Zn–air batteries has achieved remarkable results. Compared to δ-MnO_2 and α-MnO_2, the peak power density of the composites is improved by about 2 and 4 times, respectively, demonstrating excellent electrochemical properties as illustrated in Fig. 5f. Although the $(\alpha+\delta)$-Mn11 material exhibits superior catalytic properties to those of single crystal structure materials, there are still some limitations in its stability under high current density conditions. Specifically, the $(\alpha+\delta)$-Mn11-based zinc–air battery is only able to operate stably for about 200 min at the current density of 20 mA cm^{-2}. This suggests that despite the improved electrocatalytic performance of the material, its long-time cycling stability needs to be further optimized. Future research should pay more attention to this issue, and further improve the cycle life and stability of the materials by adjusting their synthesis methods or structural design, to meet the needs of practical applications.

In contrast to crystalline materials, amorphous materials are short-range ordered as metastable states. This property gives the amorphous material more randomly oriented bonds, which causes structural flexibility and exposure of defects on the surface, thus optimizing the adsorption and desorption processes of reactive substances and intermediates, thus further enhancing its catalytic efficiency. However, the short-range ordered structure usually provides more scattering towards electron transfer, leading to poor conductivity than the crystalline one. Moreover, as a kind of metastable state, the stability of amorphous materials is also a problem, especially when encountering the inevitable surface reconstruction. Therefore, the compositing of amorphous and crystalline phases has been one of the most promising strategies to tackle those problems. Through the oxidation of Mn^{2+}, Zhou and co-workers prepared an amorphous/crystalline layered manganese oxide (ACMO).[64] This ACMO not only has active lattice oxygen, which can provide active participating sites in electrochemical reactions but also possesses flexible oxygen vacancies, which can promote molecular activation during the reaction process, thus greatly enhancing the electrochemical activity of the material. In addition, ACMO is also rich in unsaturated Mn active sites, which can efficiently catalyze electrochemical reactions and enable the material to exhibit excellent performance in energy conversion and storage. Compared with well-crystallized layered MnO_2 and amorphous MnO_2, ACMO exhibits significant advantages in electrochemical performance and offers new possibilities for future energy conversion and storage technologies. As a result, the ACMO electrode exhibits remarkably high ORR activity, such as a more favorable $E_{1/2}$ value and a significantly greater limiting current density as depicted in Fig. 5g, which surpasses the pure amorphous manganese oxide (AMO) and pure crystalline layered manganese oxide (CMO). For the OER, the ACMO sample displays a lower overpotential (407 mV) than that of the AMO and CMO at 10 mA cm^{-2} in Fig. 5h. Especially, the rechargeable zinc–air battery utilizing ACMO for its air electrode possesses better electrochemical stability compared to 20% Pt/C, which enables it operating up to 1000 cycles ($\approx$17 days) at 10 mA cm^{-2} (Fig. 5i). Through in-depth exploration of the structural properties of the combined amorphous and crystalline structure, this study reveals the potential advantages of this combined structure in terms of electrochemical activity, providing practical guidance on how to enhance the electrochemical activity of the materials while maintaining their stability. The results of the study not only open up new ideas for the design of oxide materials but also provide strong support for the innovation and optimization of electrocatalytic materials in the future.

As is well known, manganese dioxide exhibits a diverse range of structures in nature due to the flexible arrangement of MnO_6 structural units, each possessing different catalytic properties. Among these, α-MnO_2 nanowires are produced via a hydrothermal process with tunneling structures, and more trivalent manganese and oxygen vacancies demonstrate great potential as ORR and OER electrocatalysts for zinc–air batteries. Additionally, the controlled synthesis of amorphous/crystalline manganese oxides can improve the number of active sites and oxygen vacancies, thereby facilitating their catalytic activity. However, the electrical conductivity of these structures may not be optimal and amorphous manganese dioxide is inherently unstable and prone to agglomeration during the reaction.

2.2 Control of morphology

Since the catalytic performance mainly depends on the surface state of the electrocatalyst,[65] morphology engineering can tune the activity of MnO_2 in two ways: optimizing the surface area and controlling different exposed surfaces.[66] Thanks to the diversity of morphological structures and synthesis methods, MnO_2 with different morphologies or large surface areas, such as nanowires,[67] nanosheets[68] and nanoflowers,[69] could be easily obtained.

2.2.1 ORR performance. Shao and others synthesized rod-like α-MnO_2 (Fig. 6a) by a hydrothermal method at different temperatures.[70] The Mn^{3+} content in α-MnO_2-120 (the reaction temperature of 120 °C) is high, and the oxygen vacancy is abundant. The one-dimensional rod-like α-MnO_2-120 possesses a large specific surface area, which can provide a larger electrochemically active region and more active sites. It is found that α-MnO_2-120 exhibits outstanding catalytic performance through four electronic pathways during the ORR process. The catalyst exhibits a large half-wave potential of 0.85 V comparable to that of commercial Pt/C. Meanwhile, the diffusion-limiting current of the α-MnO_2-120 catalyst is also superior to that of commercial Pt/C, showing its excellent electrochemical properties as shown in Fig. 6b. Furthermore, electrochemical tests show that the α-MnO_2-120 catalyst used in zinc–air batteries displays satisfactory results, such as a maximum power density of 240 mW cm^{-2} as illustrated in Fig. 6c. This study provides an important pathway for the development of more efficient Mn-based ORR catalysts. In addition, the catalyst shows good potential for application in zinc–air batteries, exhibiting excellent electrochemical performance and practical application value. In the future, by further optimizing the OER performance of this catalyst, it is expected to be developed into a bifunctional catalyst with both ORR and OER activities, leading to more efficient and stable zinc–air batteries.

Cheng successfully synthesized 3D hierarchical hollow β-MnO_2 microspheres (H-β-MnO_2) assembled from nanorods as illustrated in Fig. 6d by a one-step hydrothermal method.[71] The homogeneous hollow microspheres with large cavities not only can shorten the molecular/ionic diffusion distance for surface reactions but also inhibit the aggregation of particles. The H-β-MnO_2 sample boasts a surface with a higher concentration of oxygen vacancies, enhancing its capacity to adsorb and activate oxygen molecules. This feature is advantageous for various chemical reactions and processes that rely on the efficient utilization of oxygen. Compared with commercial β-MnO_2 particles (C-β-MnO_2), the H-β-MnO_2 electrode displays better ORR electrocatalytic activity, achieving a higher half-wave potential, a greater limiting current density and high current retention after 5 hours of durability testing as shown in Fig. 6e and f, respectively. This work not only provides a facile and reliable synthetic route for the preparation of layered hollow MnO_2 crystals but also deeply reveals its unique growth mechanism, which helps researchers to better understand the formation process of hollow structures.

2.2.2 OER performance. Zhou prepared MnO_2 nanosheets with abundant oxygen vacancies (V_O-MnO_2-NF) by an uncomplicated *in situ* hydrothermal growth process and electrochemical oxidation treatment as described in Fig. 7a.[72] The porous structure of the reassembled nanosheets and nanoflowers provides a larger surface area and a higher number of
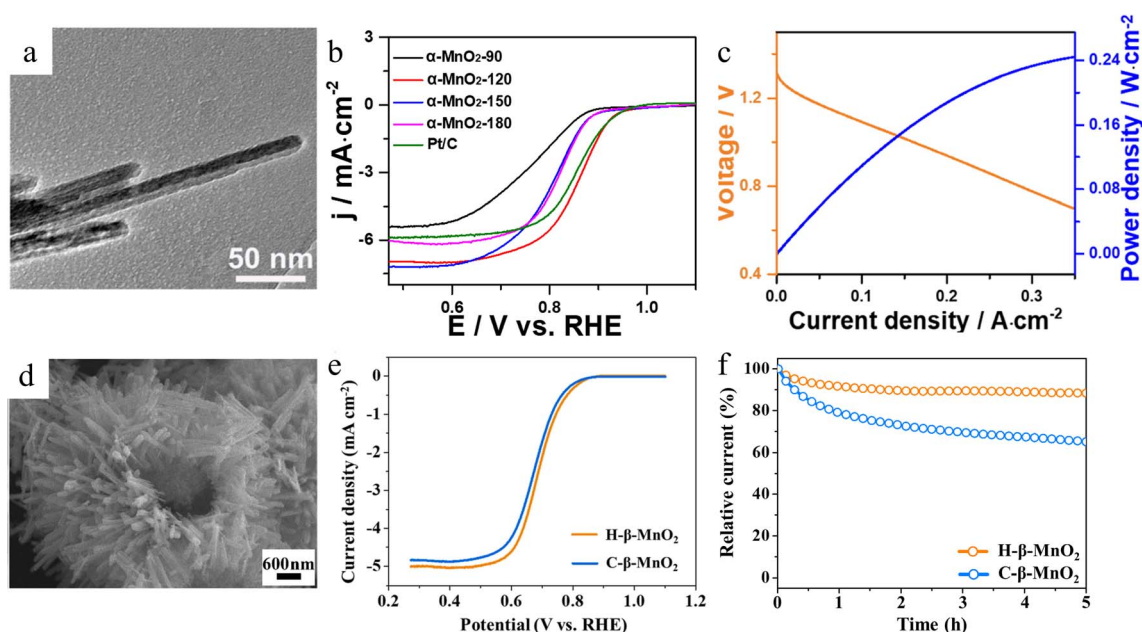

Fig. 6 The surface morphology and ORR performance of α-MnO_2 and H-β-MnO_2. (a) Morphology of α-MnO_2-120. (b) ORR polarization curves of the obtained samples. (c) Discharge polarization and the corresponding power density curves of the Zn–air batteries with α-MnO_2-120 as catalyst. Reproduced with permission.[70] Copyright 2021, Elsevier. (d) SEM image of H-β-MnO_2. (e) LSV curves of β-MnO_2 samples. (f) Chronoamperometric responses of the H-β-MnO_2 and C-β-MnO_2 samples. Reproduced with permission.[71] Copyright 2022, Elsevier.

29362 | *J. Mater. Chem. A*, 2024, **12**, 29355–29382

This journal is © The Royal Society of Chemistry 2024

Mn^{3+}. Electrochemical oxidation treatment can produce a large number of oxygen vacancies, which has a positive effect on improving the kinetics of OER activity. The synthesized V_O-MnO_2-NF sample has been an effective electrocatalyst for the OER with lower overpotential, minimal Tafel slope, smaller charge-transfer resistance and perfect stability (Fig. 7b–d). This study demonstrates a feasible approach to fabricating an efficient OER catalyst, highlighting the great potential of the VO-MnO_2-NF material with a porous structure and a large specific surface area. The unique structure of this catalyst not only enhances its electrochemical performance but also provides an important reference and inspiration for the development of more reliable and efficient catalysts in the future. Further studies could use electron donation effects and band gap engineering to optimize catalyst performance.

Chen reported an unusual network of α-MnO_2 nanowires (Fig. 7e) synthesized by a mild hydrothermal reaction in the absence of any surfactant.[73] In this network, the nanowires are interconnected from all directions through nodes, which are connected infinitely node by node to form a 3D network structure. α-MnO_2 nanowire networks (α-MnO_2-NWN) are highly hydrophilic due to the large number of interstitial spaces induced by the structure. Charge transfer in the network structure is much faster than randomly stacked nanowires and balls. The unique network structure of α-MnO_2 nanowires possesses better hydrophilicity and electrical conductivity, making it a powerful OER electrocatalyst, exhibiting a smaller overpotential of 468 mV, a lower Tafel slope, and the ability to be stable for more than ten hours at 8 mA cm^{-2} (Fig. 7f–h). This study not only provides an innovative synthetic route for building advanced network-structured materials but also opens up new horizons for the design of electrochemical materials. By optimizing the structure, researchers succeeded in designing catalysts with efficient mass diffusion and charge transfer functions, which significantly enhanced the electrochemical performance. These findings provide new perspectives for understanding and improving the working mechanism of MnO_2 catalysts and may provide lessons for the design of other oxide catalysts.

2.2.3 ORR & OER performance in a zinc–air battery. The preparation of MnO_2 in different morphologies is a relatively simple and efficient process. Whether it is MnO_2 nanoparticles,
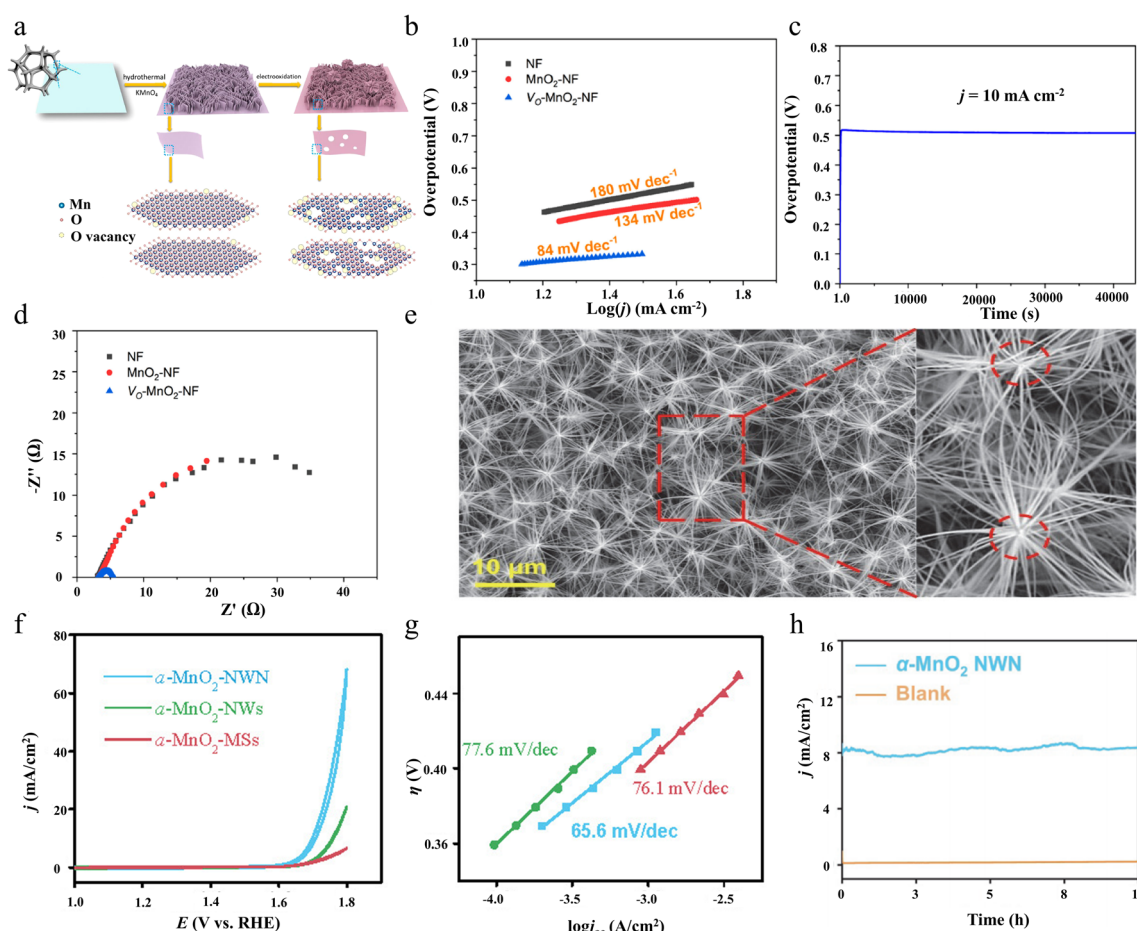

Fig. 7 The preparation method and OER performance of V_O-MnO_2-NF. The morphology and OER performance of the α-MnO_2 nanowire network. (a) Preparation process of the V_O-MnO_2-NF sample. (b) Tafel plots. (c) Stability test for V_O-MnO_2-NF. (d) Nyquist plots of the obtained samples at 1.6 V (*vs.* RHE) without *iR* compensation. Reproduced with permission.[72] Copyright 2021, Elsevier. (e) The morphology of the α-MnO_2-NWN. (f) LSVs of the three α-MnO_2 materials. (g) Tafel plots. (h) The CPE of water for the OER from the α-MnO_2-NWN at 1.7 V for 10 h in a 1 M KOH. Reproduced with permission.[73] Copyright 2021, Elsevier.

This journal is © The Royal Society of Chemistry 2024

J. Mater. Chem. A, 2024, **12**, 29355–29382 | **29363**

nanowires, nanosheets, or even nanospheres, the preparation process can be realized by adjusting the synthesis conditions, such as temperature, pressure, the ratio of reactants, and the introduction of different templating agents or additives. Each unique morphology contributes significantly to increasing the total surface area of the catalyst. The increased surface area means that more active sites are exposed, providing more contact points for the reaction. When MnO_2 is used as a bifunctional catalyst for zinc–air batteries, these contact sites not only effectively promote the electrochemical reactions within the battery, but also increase the rate and efficiency of the reactions.

Song and coworkers reported a simple hydrothermal synthesis method to prepare $TiC/\alpha\text{-}MnO_2$ nanowires ($TiC/\alpha\text{-}MnO_2NW$) at low temperatures.[74] One-dimensional $\alpha\text{-}MnO_2$ nanowires overlap and intersect, resulting in the formation of scaffolds, which facilitates electron transport. The TiC nanoparticles with stable structure and high electrical conductivity are uniformly dispersed on the Mn nanowires as depicted in Fig. 8a, leading to an effective increase in electronic conductivity and further contributing to charge transfer. Because of the abundance of active sites on the high specific surface area of $\alpha\text{-}MnO_2$ nanowires, the $TiC/\alpha\text{-}MnO_2NW$ electrocatalysts on the cathode of zinc–air batteries exhibit good bifunctional properties. As shown in Fig. 8b, $TiC/\alpha\text{-}MnO_2NW$ exhibits similar ORR performance to Pt/C with a comparable original potential, half-wave potential and limiting current density. Not only that, the OER potential of $TiC/\alpha\text{-}MnO_2NW$ is significantly lower than that of IrO_2 at 10 mA cm^{-2} (Fig. 8c). Importantly, The $TiC/\alpha\text{-}MnO_2NW$-assembled zinc–air battery shows excellent power density, reaching a peak value of 161.3 mW cm^{-2} (Fig. 8d). And this battery is capable of stable operation at 20 mA cm^{-2} for 5000 minutes. This demonstrates the wide application of one-dimensional nanowire materials in electrocatalysis. The development of $TiC/\alpha\text{-}MnO_2$ nanowire (NW) materials provides a promising strategy for the design of bifunctional oxygen electrocatalysts with long-lasting and high activity.

Bang Lan et al. successfully synthesized 3D hollow urchin-like $\alpha\text{-}MnO_2$ microspheres by a simple hydrothermal method.[75] The distinctive morphology allows abundant active sites to be exposed in the reaction environment and enhances intrinsic activity as well as accelerating electron transfer. In electrochemical performance tests, the urchin-like $\alpha\text{-}MnO_2$ shows impressive performance. It exhibits outstanding ORR performance as shown in Fig. 8f, demonstrating great potential for energy conversion and storage. Meanwhile, Fig. 8g shows that it also exhibits excellent OER activity with a low over-potential at the current density of 10 mA cm^{-2}, which further validates its excellent electrochemical performance. What's more, the rechargeable zinc–air battery that employs the urchin-like $\alpha\text{-}MnO_2$ displays remarkable performance with higher open-circuit voltage (Fig. 8h) and larger power density(Fig. 8i) in comparison to other morphologies of MnO_2, which can be widely used in practice. The hollow $\alpha\text{-}MnO_2$ based rechargeable zinc–air battery shows a small cycling voltage gap between the charge and discharge platforms after 400 cycles. Bifunctional catalysts with good stability and cost-effectiveness are

successfully prepared by innovative morphology design to enhance the electrochemical performance of MnO_2 materials in zinc–air batteries.

All in all, the electrocatalytic activity of MnO_2 is strongly influenced by its crystal surface. The formation of two/three-dimensional nanosheet, nanoflower and nanosphere structures can increase the surface area, thereby accelerating electron transport, which can expose more active sites that participate in the catalytic process and promote catalytic activity. The synthesized $\alpha\text{-}MnO_2$ microspheres with a unique three-dimensional hollow urchin-like structure have rich accessible active sites and enhance intrinsic activity, exhibiting superior electrochemical properties as cathodes of zinc–air batteries. Therefore, preparing different forms of MnO_2 can not only enrich the types and properties of catalysts but can also optimize its application effect in zinc–air batteries, which can provide strong support for the performance enhancement and practical application of batteries.

2.3 Heteroatom-doped manganese dioxide

The low conductivity of the MnO_x catalysts is one of the aspects that limit their application in zinc–air batteries.[57] One way to overcome this problem is to accelerate the electron transfer of MnO_x by doping it with heteroatoms (e.g., Co,[76] Ni,[77] Fe,[78] Al,[79] Ag[80]). Doping is one of the common methods to modulate the intrinsic local electronic structure of metal oxides.[81] As reported, the doping of heteroatoms into MnO_2 not only effectively modulates its electronic structure and surface properties, but also generates additional active sites for the ORR/OER, thus improving electrocatalytic performance.[82,83] What's more, it is important to choose a suitable dopant. Generally, the ionic radius of the dopant should be close to that of the Mn ion, which ensures the stability of the lattice after doping and helps to reduce the lattice distortion. The redox potential of the dopant should be coordinated with the redox potential of Mn to facilitate the charge transfer process and thus enhance the electrochemical properties. The incorporation of dopants should help to modulate the electronic structure of MnO_2 to improve its electrical conductivity and catalytic activity. In addition, the dopant should be chemically stable under operating conditions to ensure the long-term stability and durability of the electrocatalyst. Besides, the catalytic activity of MnO_2 varies with different doping sites even for the same dopant.[84]

2.3.1 ORR performance. Some dopants alter the valence states of Mn to enhance its ORR activity. As an example, Zhou et al. synthesized $\alpha\text{-}MnO_2$ ($Cu\text{-}\alpha\text{-}MnO_2$) nanowires doped with different Cu^{2+} ion contents by a hydrothermal method.[85] The substitution of larger Cu^{2+} for Mn^{3+} (0.645 Å) or Mn^{4+} (0.530 Å) leads to lattice expansion and increases the amount of Mn^{3+}. The addition of Cu ions resulted in enhanced reaction kinetics. The performance of $Cu\text{-}\alpha\text{-}MnO_2$ nanowires exhibits excellent ORR activity compared to undoped $\alpha\text{-}MnO_2$ nanowires. As depicted in Fig. 9a, the onset potential and half-wave potential of $Cu\text{-}\alpha\text{-}MnO_2$ (Cu : Mn = 1 : 4, the molar ratio of Cu and Mn is 1 to 4) are more positive than those of the undoped $\alpha\text{-}MnO_2$ nanowires. Moreover, the limiting current density of $Cu\text{-}\alpha\text{-}$

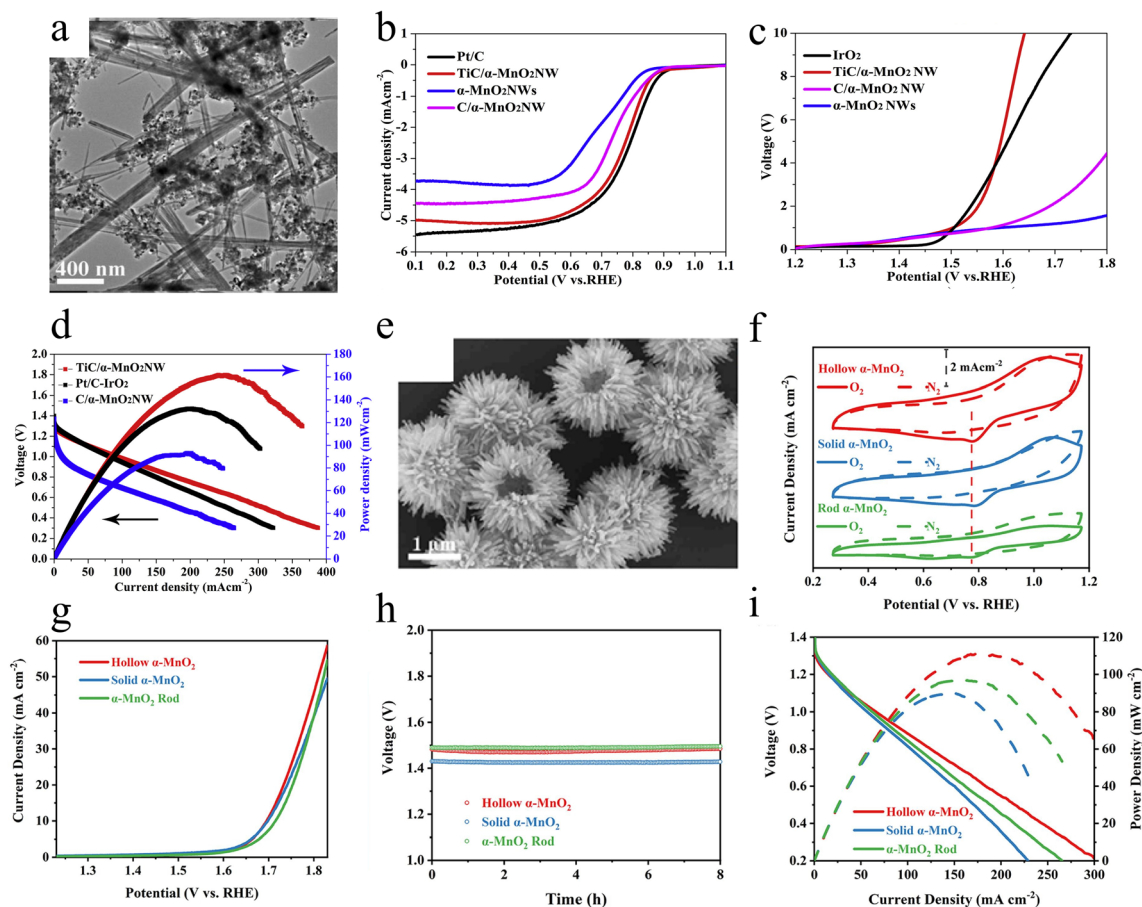29364 | J. Mater. Chem. A, 2024, 12, 29355–29382

This journal is © The Royal Society of Chemistry 2024

Fig. 8 The surface morphology and electrocatalytic performance. (a) The SEM image of TiC/α-MnO$_2$NW prepared by a hydrothermal method. (b) LSV curves for the ORR, (c) LSV curves for the OER, and (d) discharge polarization curves of various catalysts. Reproduced with permission.[74] Copyright 2020, Elsevier. (e) The SEM image of the urchin-like α-MnO$_2$ prepared by a hydrothermal method. (f) CV polarization curves. (g) OER polarization curves. (h) Open-circuit plots, and (i) the discharge polarization curves and power density plots of the assembled zinc−air battery. Reproduced with permission.[75] Copyright 2022, Elsevier.

MnO$_2$ (Cu : Mn = 1 : 4) is only slightly smaller than that of the benchmark electrocatalyst. The Cu–α-MnO$_2$ (Cu : Mn = 1 : 4) sample shows fast reaction kinetics, achieving a much smaller Tafel slope than α-MnO$_2$ which is closer to that of commercial Pt/C and the charge transfer resistance is much smaller, suggesting that it is a fairly active ORR catalyst as shown in Fig. 9b and c, respectively. Cheap and efficient ORR catalysts are synthesized by simple Cu ion doping, which successfully improves the electrocatalytic performance of α-MnO$_2$ nanowires in Mg–air batteries. Future research still needs to focus on how to precisely control the doping concentration and homogeneity as well as its application in zinc–air batteries.

In addition to the doping of a single metal element, the synergistic effect of doping of a variety of metal elements can further increase the ORR performance of the catalyst, which is beyond the effect that can be achieved by any one metal alone. This synergistic effect not only originates from the complex electronic interactions between multiple metal elements but also from their optimization of the catalyst geometry and chemical environment. This optimization has allowed the catalysts to exhibit higher activity and stability in the ORR,

providing strong support for the development of energy conversion devices. Jin *et al.* successfully reported a facile two-step solution method as described in Fig. 9d to design α-MnO$_2$ nanorods intercalated by Ag$^+$ into the tunnel and then loaded by trace Cr(OH)$_3$ (denoted as Cr/AMO), which can enhance the electrocatalytic activity.[86] By introducing Ag$^+$ into the structure of α-MnO$_2$, its catalytic properties are bolstered, resulting in improved reactivity and efficiency. Meanwhile, the trace amount of Cr(OH)$_3$ loaded on the surface of α-MnO$_2$ effectively increased the electrochemically active surface area, thereby facilitating electron transfer and improving electrochemical performance. These modifications collectively contribute to the overall improvement of the performance of α-MnO$_2$ in catalytic and electrochemical applications. The synergistic effect of the three can accelerate electron transfer, regulate the ratio of Mn^{3+}/Mn^{4+}, and create lots of oxygen vacancies, which contribute to the adsorption and activation of O$_2$ on the surface. Compared to the reference catalyst, the obtained catalyst (Cr/AMO physically mixed with Vulcan carbon (XC-72), denoted as Cr/AMO + C) displays higher half-wave potential, faster reaction kinetics and high mass activity of
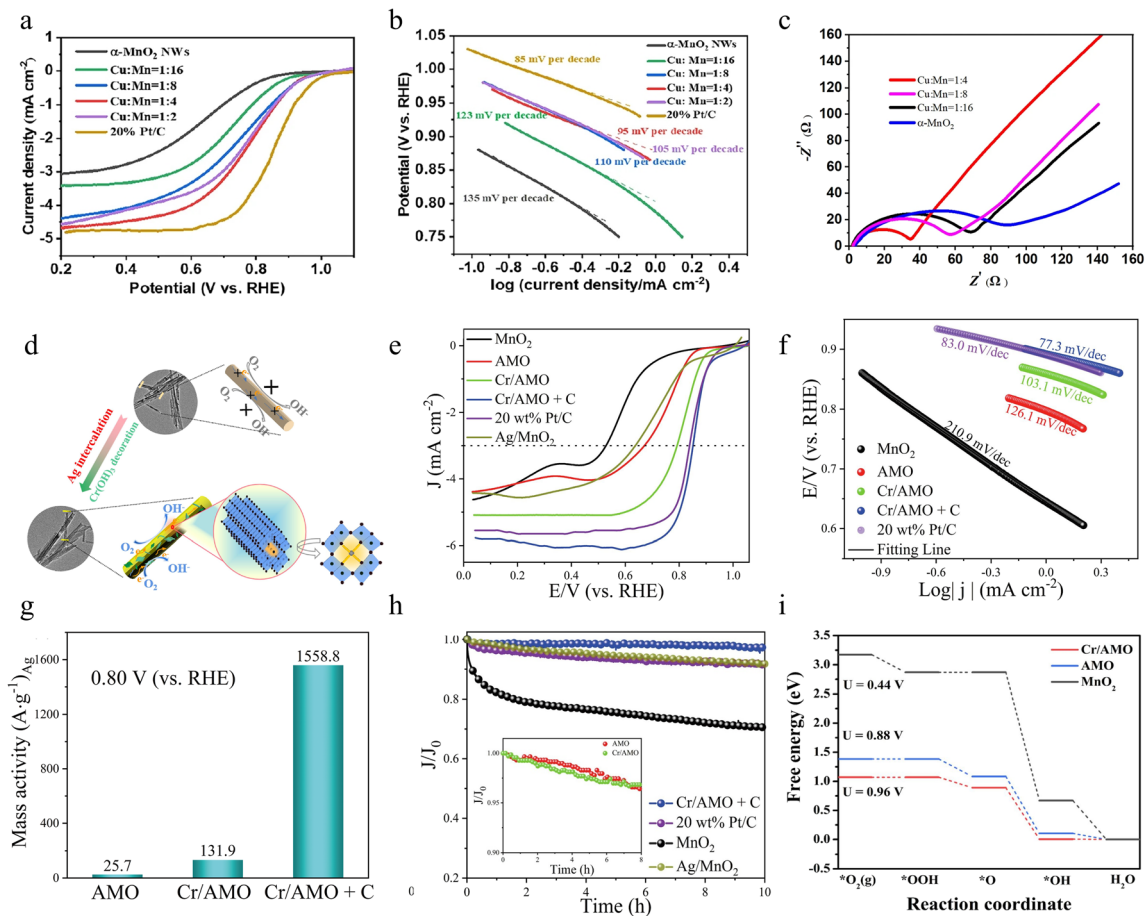
Fig. 9 The ORR performance of Cu−α-MnO$_2$ and Cr/AMO. (a) LSV curves for the ORR. (b) Tafel plots. (c) Nyquist plots of α-MnO$_2$ and the different Cu dopants of Cu−α-MnO$_2$. Reproduced with permission.[85] Copyright 2021, Springer Nature. (d) Synergistic catalytic mechanism of Cr/AMO for the ORR. (e) LSV curves of the catalysts. (f) Tafel plots. (g) The mass activity (normalized by Ag). (h) Current time (i–t) chronoamperometric responses at 0.60 V ($vs.$ RHE) of different catalysts. (i) ORR free energy diagram of the catalysts. Reproduced with permission.[86] Copyright 2023, Elsevier.

1558.8 A g$_{Ag}^{-1}$ at 0.80 V for highly excellent ORR performance under alkaline conditions as depicted in Fig. 9e–g, respectively. Notably, Fig. 9h shows that the electrochemical current drop rate of the resulting catalyst is 3.5% after 10 h of i–t testing, which is mainly attributed to the Ag$^+$-embedded tunneling structure that well stabilized the active sites. Finally, the strong coupling interactions between MnO$_2$, Ag$^+$ and Cr(OH)$_3$ improve the ORR performance as verified by density functional theory calculations (Fig. 9i). This study provides a co-doping strategy for designing MnO$_2$-based electrocatalysts with efficient ORR. The theoretical computational analyses provide a more thorough understanding of the mechanism. This co-modification strategy not only shows obvious advantages in improving the catalytic efficiency but also achieves good results in the corrosion resistance and durability of the material.

2.3.2 OER performance. To enhance the intrinsic OER activity of the active sites of MnO$_2$, introducing special metal element doping can optimize the adsorption energy of the existing active sites. The introduction of other elements leads to changes in charge distribution and electronic structure, which reduces the energy barrier in the OER process and makes the reaction easier. In addition, metal doping increases the quantity

of active sites of MnO$_2$. When metal elements are introduced into the crystal structure of MnO$_2$, it is possible to form new active sites that have different electronic structures and chemical properties from those of pristine MnO$_2$. Therefore, more active sites can participate in the OER process and improve the overall performance of the catalyst. Salvador et $al.$ have prepared Pd/α-MnO$_2$ by introducing Pd^{2+} precursors during the synthesis of α-MnO$_2$ from Mn^{2+} and MnO$_4^-$ under reflux.[87] The Pd^{2+} precursor was oxidized by MnO$_4^-$ during the synthesis, and Pd^{4+} ions partially replaced the Mn^{3+} ions in the α-MnO$_2$ lattice due to the similarity of the radius of the Pd^{4+} and Mn^{3+} ions. This lattice framework substitution results in an increase in the average oxidation state of Mn, a decrease in the crystallite size of the nano-oxides, and an increase in the surface area. In addition, PdO is also deposited on the oxide surface. The presence of PdO and Pd^{4+} ions leads to the reduction of charge transfer resistance, thereby strengthening the OER activity of MnO$_2$. As shown in Fig. 10a and b, Pd/α-MnO$_2$ also exhibits superior overpotential at 10 mA cm^{-2} current density, excellent reaction stability and lower Tafel slope than the pure MnO$_2$ in this work, which may be ascribable to the higher reduction potential of Pd^{4+} compared to Mn^{4+} and Mn^{3+}, as well as oxygen surface
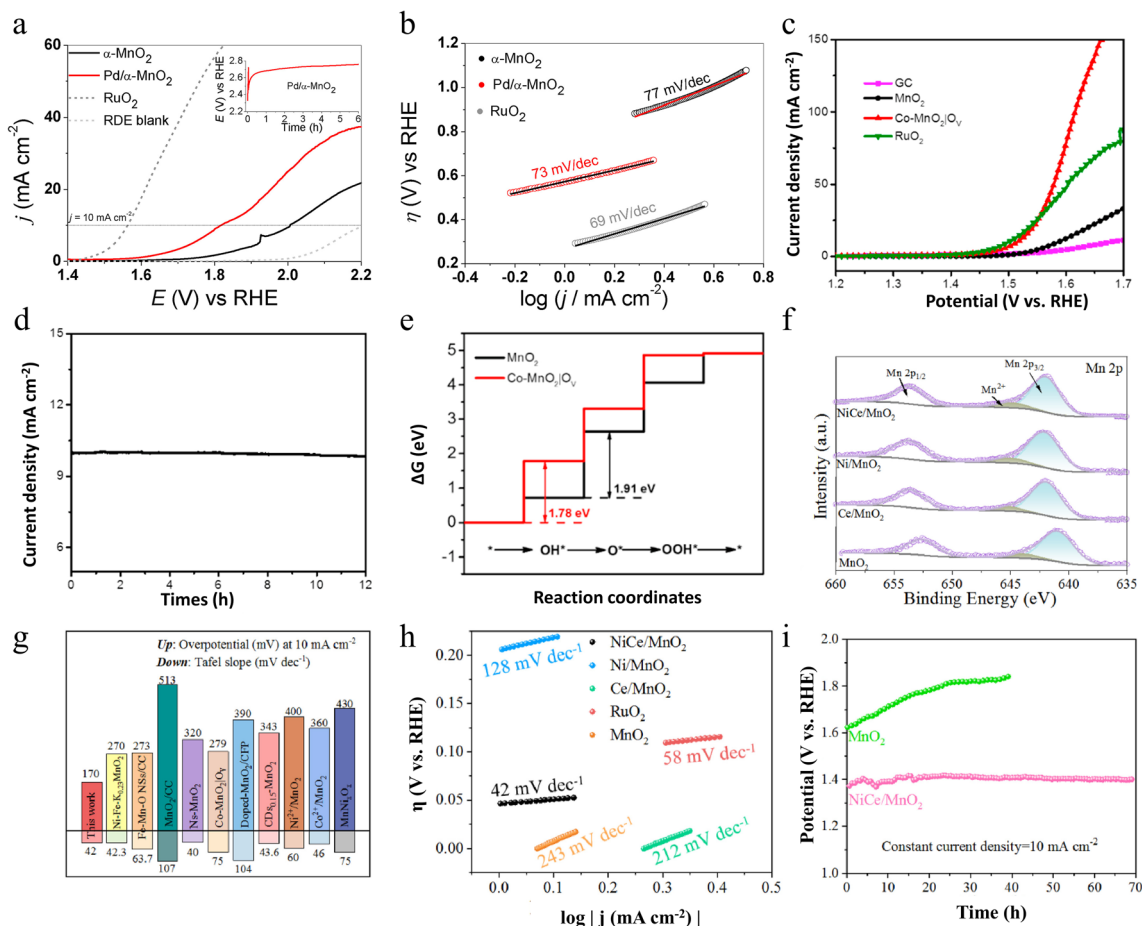
Fig. 10 The OER performance of Pd/α-MnO₂, Co–MnO₂|OV and NiCe/MnO₂. (a) LSV curves and (b) Tafel plots of α-MnO₂, Pd/α-MnO₂ and RuO₂. Reproduced with permission.[87] Copyright 2021, Elsevier. (c) Polarization curves and (d) time dependence of catalytic current density during electrolysis at a static potential of Co–MnO₂|OV. (e) Reaction coordinates of the OER on MnO₂ and Co–MnO₂|OV. Reproduced with permission.[88] Copyright 2018, Elsevier. (f) Mn 2p of MnO₂, Ni/MnO₂, Ce/MnO₂ and NiCe/MnO₂. (g) Comparison with recently reported MnO₂-based catalysts. (h) Tafel slopes and (i) the stability tests of NiCe/MnO₂ at 10 mA cm⁻² of MnO₂, Ce/MnO₂, Ni/MnO₂, NiCe/MnO₂ and RuO₂. Reproduced with permission.[89] Copyright 2023, Elsevier.

enrichment. In conclusion, although Pd^{4+}-doped α-MnO₂ is still inferior to RuO₂ in terms of OER performance, its advantages in terms of material cost and resource availability make this study of significant application value. Future studies can further optimize the Pd doping method and enhance its catalytic performance to be closer to or even exceed the existing benchmark catalysts.

In addition to doping with Pd cations, introducing metal ions such as Fe, Ni, and Co into MnO₂ is an effective strategy to enhance the catalytic performance of the oxygen evolution reaction. Zhao and colleagues first synthesized cobalt/nitrogen co-functionalized carbon nanofibers (Co/NCNFs) using an electrospinning method, followed by an annealing treatment for 8 hours in a mixed H₂/Ar atmosphere.[88] Subsequently, they produced cobalt-doped ultrathin manganese dioxide nanosheets, rich in oxygen vacancies, which were vertically aligned on the functionalized carbon nanofibers (Co–MnO₂|OV) through a spontaneous redox reaction between Co/NCNFs and KMnO₄. Notably, Co played a crucial role during the second redox reaction step, significantly enhancing the formation of

ultrathin and ultra-long MnO₂ nanosheets. Co-functionalized carbon nanofiber conductive substrates and Co ion doping as well as oxygen vacancies greatly enhance the efficiency of electron transfer. Not only that, the strong synergistic coupling effect between Co and MnO₂ further enhances the overall performance of the material. Importantly, its ultrathin two-dimensional morphology and a large number of oxygen vacancies provide more active sites for the OER. Thanks to these synergistic advantages, the Co–MnO₂|OV composites exhibit excellent OER electrocatalytic activity and good long-term stability in alkaline electrolytes. As illustrated in Fig. 10c and d, at the current density of 10 mA cm⁻², the overpotential of Co–MnO₂|OV is only 279 mV, which is much lower than that of untreated MnO₂, and it can operate stably for 12 h at this current. Density Functional Theory (DFT) calculations further show that Co-doped MnO₂ with oxygen vacancies on the surface can adjust the rate-determining step of the OER from "*OH to *O" (pure MnO₂) to the formation of *OH adsorption intermediates with a lower free energy gap as depicted in Fig. 10e. This simple redox method is not only extremely tractable but also

This journal is © The Royal Society of Chemistry 2024

J. Mater. Chem. A, 2024, **12**, 29355–29382 | **29367**

easily extendable to the preparation of other ion (*e.g.*, Fe, Ni, *etc.*) doped metal oxides. Through this method, not only can efficient OER be realized, but it can also be widely used in other energy conversion and storage technologies, such as Li-ion batteries, supercapacitors, and fuel cells. This method provides a flexible and efficient way to develop new functional materials and demonstrates great potential for application in energy science and technology.

In the OER, co-dopants usually play multiple functions. Zhang and co-workers reported Ce and Ni co-doped MnO_2 ($NiCe/MnO_2$) nanosheets (NSs) with abundant active sites and lots of oxygen vacancies (V_O) by a defect engineering strategy.[89] On one side, the introduction of Ni and Ce reduces production size, increases the specific surface area, and facilitates the exposure of a greater number of active sites. From another perspective, additional electrons or electron transfer effects introduced by Ce/Ni doping affect the valence state and the surrounding chemical environment of Mn ions, leading to significant changes in the electronic structure of Mn^{3+} and Mn^{4+}, altering the substance on the crystal surface and stimulating the formation of Vo, which simultaneously activates the OER properties of the obtained catalyst (Fig. 10f). The OER properties of $NiCe/MnO_2$ NSs are remarkably strengthened compared to those of δ-MnO_2, reaching a lower overpotential of 170 mV (10 mA cm^{-2}) and faster reaction kinetics, which is close to that of RuO_2, as well as excellent stability with negligible drop in efficacy after cycling (Fig. 10g–i). Overall, this work not only provides a new avenue for research into designing high-performance OER catalysts but also provides strong support for the promotion and application of non-precious metal catalysts in practical industrial applications.

2.3.3   ORR & OER performance in a zinc–air battery. The above exhaustive findings indicate that doping technology plays a crucial role in the enhancement of the ORR and OER performance of electrocatalysts. The electronic structure of electrocatalysts can be effectively changed by introducing different kinds of doping elements. The adjustment of the electronic structure can optimize the interaction between the catalyst and the reactants, thus improving the catalytic activity and selectivity of the catalyst. Doping not only adjusts the electronic structure but also regulates the adsorption barrier and activation energy during the reaction. This means that in electrochemical reactions, doped catalysts can adsorb and activate reactants more efficiently, reducing the energy required for the reaction and making it easier to proceed. In addition, the doping technique can significantly increase the conductivity of the electrocatalyst, so that the charge transfer inside the catalyst is smoother.

Due to high atom utilization, selectivity and catalytic activity, heterogeneous electrocatalysts characterized by single atoms or atom dispersion have been extensively investigated in various chemical transformations. Ni *et al.* synthesized single-atom Ag-doped MnO_2 nanowires (denoted as Ag-MnO_2) with bifunctional electrocatalytic activity by a hydrothermal method.[90] The Ag dopant significantly improved the electrical conductivity of MnO_2 and induced the lattice distortion of MnO_2 to introduce more oxygen vacancies, which could generate more reactive

sites and enhance the oxygen electrocatalytic performance. Remarkably, the Ag–MnO_2 based zinc–air batteries can be operated stably for up to 3200 charging/discharging cycles. Xiang *et al.* introduced Pd single atoms into the three-dimensional interwoven structure of MnO_2 nanowires and carbon nanotubes (Pd/MnO_2-CNT).[91] The Pd single atoms have a synergistic effect with the Mn sites around the MnO_2 surface to optimize the binding energy of the reaction intermediates. The Pd/MnO_2-CNT exhibits promising ORR and OER bifunctional electrocatalytic performances and outstanding stability in an alkaline electrolyte. The zinc–air battery assembled by the Pd/MnO_2-CNT exhibits high power density, excellent rate performance, and good cycling stability. In addition, the preparation method is simple and this strategy is not only applicable to current catalytic systems but can be further extended to design efficient atomically dispersed electrocatalysts using the unique electronic interactions between isolated atoms and metal oxide supports. Through this approach, various functions can be achieved, such as improving the activity, selectivity and stability of the catalysts, which are suitable for a wide range of electrochemical reactions including water decomposition and CO_2 reduction reactions, showing a wide range of potential applications.

In addition to single-atom doping, the introduction of cations into MnO_2 is a commonly used strategy. Bôas N. V. *et al.* prepared Bi^{3+} or Ce^{4+} doped manganese dioxide nanorods exhibiting higher electrical conductivity *via* a one-step hydrothermal process.[92] The doped cations are in the water molecule-filled tunnels. The doping of Bi^{3+} and Ce^{4+} allows the α-MnO_2 recognized as octahedral molecular sieves (OMS-2) to possess a lower bandgap value in comparison with K^+ doped α-MnO_2. This property means that electrons encounter less obstruction when moving inside the material, and as a result, Bi^{3+} and Ce^{4+} doped α-MnO_2 exhibit higher electrical conductivity. Based on the study of Bi^{3+} and Ce^{4+} doped α-MnO_2 catalysts, both of them show excellent performance in the ORR. As shown in Fig. 11a, the activity of these catalysts in the ORR process is significantly higher than that of the conventional Pt/C catalyst, showing a trend toward a more positive reaction. The value of ΔE_{Bi} (the discrepancy in potential between the $E_{j=10}$ during the OER and the $E_{1/2}$ encountered during the ORR) is 1.07 V and ΔE_{Ce} is 1.02 V (Fig. 11b), and both of them are very nearly the same as the good OER catalysts that have been reported. What's more, zinc–air microcell tests confirmed the excellent catalytic performance. BiOMS-2 and CeOMS-2 show good stability, and the potential value is almost always constant in Fig. 11c. In conclusion, the doping of Bi^{3+} or Ce^{4+} not only improves the activity of the catalyst but also significantly enhances its stability under an electrochemical environment. However, the charge–discharge cycling stability of this catalyst in zinc–air batteries needs to be explored. Bi, as a rare element, has a relatively high cost, so it may affect the overall economy of the material in practical applications.

Besides single metal doping, Mathur *et al.* sequentially introduced Fe and Ni into 2D layered MnO_2 (NiFeMn) *via* a hydrothermal method.[93] Fe and Ni occupy the crystal surface space and interlayer region of MnO_2, changing the electronic

29368 | *J. Mater. Chem. A*, 2024, **12**, 29355–29382

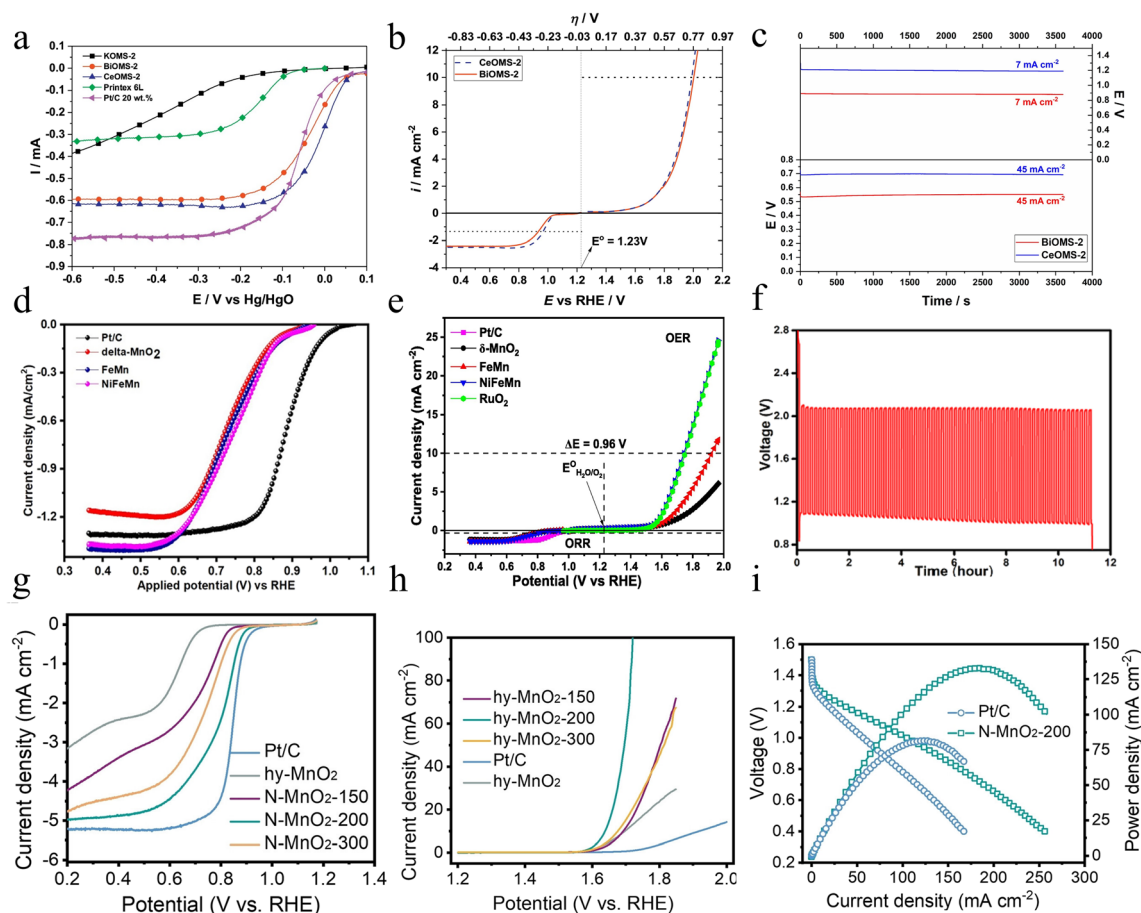This journal is © The Royal Society of Chemistry 2024

Fig. 11 The electrocatalytic performance of manganese dioxide doped with different elements. (a) Polarization curves for the ORR, (b) polarization curves for the OER, and (c) potential–time plots of the Bi- and Ce-doped MnO_2 prepared by a hydrothermal method. Reproduced with permission.[92] Copyright 2019, Elsevier. (d) ORR curves and (e) OER curves of different electrocatalysts. (f) Galvanostatic charge–discharge plot taken at 10 mA cm^{-2} of NiFeMn prepared by a hydrothermal method. Reproduced with permission.[93] Copyright 2023, Elsevier. (g) LSV curves for the ORR, (h) LSV curves for the OER, and (i) Polarization and power density curves of hy-MnO_2 and N-MnO_2-T prepared by the calcining method and Pt/C. Reproduced with permission.[94] Copyright 2023, Wiley-VCH.

structure of the MnO_2 lattice and thus generating new energy levels. In addition, Fe–Ni co-doping not only increases the electronic conductivity, leading to faster reaction kinetics but also introduces more ORR as well as OER active sites, which can bring better catalytic effects. The co-existence of Fe, Ni, and Mn in the form of redox pairs is an important factor in guaranteeing superior electrocatalytic performance. In conclusion, the positive synergistic effects of the dopants Fe and Ni display suitable absorption energies for *O and *OH intermediates and optimize the overall electrocatalytic activity of MnO_2. In the ORR, NiFeMn performs better than undoped δ-MnO_2, with a higher half-wave potential ($E_{1/2}$) and larger diffusion-limited current density, as Fig. 11d shows. For the OER, NiFeMn has a smaller overpotential compared to undoped and singly doped samples as demonstrated in Fig. 11e. Importantly, the ΔE (potential difference at 10 mA cm^{-2} in the OER and −0.3 mA cm^{-2} in the ORR) is only 0.93 V, showing the good bifunctional performance of the NiFeMn electrode. What's more, rechargeable zinc–air batteries with NiFeMn as the cathode show excellent charge and discharge performance, outstanding cycle performance and durability as shown in Fig. 11f. In conclusion, the Ni and Fe

doped δ-MnO_2 catalysts not only exhibit excellent catalytic activity in the OER and ORR by their highly porous structure and enhanced electrical conductivity, but also show great potential as electrodes for rechargeable zinc–air batteries. In the future, research based on this material can further optimize its structural properties, leading to the development of more efficient and low-cost electrocatalysts to promote the technological advancement of new energy storage devices such as zinc–air batteries.

In addition to metal doping, manganese dioxide can also be doped with nonmetal which can be used to substitute oxygen atoms in MnO_2, thus tuning its intrinsic properties (crystal structure or electronic structure) and consequently enhancing electrocatalytic activity. Moreover, as the p–d orbital hybridization usually promotes the breaking of the scaling effect, nonmetal doping is more prone to enhance the OER and ORR simultaneously.[95] Zhang *et al.* prepared N-MnO_2-200 *via* calcining for 2 h in a 2% NH_3 atmosphere.[94] N-doping effectively changes the microstructure of the catalyst, resulting in a significant increase in its surface area. The larger surface area means that the catalyst can make wider contact with the

This journal is © The Royal Society of Chemistry 2024

J. Mater. Chem. A, 2024, **12**, 29355–29382 | **29369**

reactants, thus improving the catalytic efficiency. This increased surface area provides more active sites for the ORR and OER, making the reaction process more efficient. The introduction of Mn^{3+} and oxygen vacancies *via* N doping not only optimizes the structure of the catalyst, but also greatly facilitates the charge transfer, which leads to the improvement of the reaction rate and efficiency, and significantly enhances the bifunctional performance of MnO_2. As Fig. 11g shows, the N-MnO_2-200 exhibits an $E_{1/2}$ of 0.797 V and a limiting current density of 4.96 mA cm^{-2}, with electrocatalytic properties similar to those reported in recent literature for other manganese oxides, such as Ag–MnO_2 (ref. 80) (0.67 V and 4.5 mA cm^{-2}) and Ru(0.1)–MnO_2 (ref. 96) (0.85 V and 5.37 mA cm^{-2}). As seen in Fig. 11h, the N-MnO_2-200 exhibits the most remarkable OER electrocatalytic performance with a lower potential and the small ΔE value is 0.842 V, surpassing that of the hydrated manganese dioxide (hy-MnO_2) electrode. Not only that, the N-MnO_2-200 assembled zinc–air battery shows a peak power density of 132.8 mW cm^{-2} in Fig. 11i. What's more, the ZAB has excellent stability and is capable of sustaining up to 50 hours of charge/discharge cycles without being affected. In general, this work demonstrates an effective way to modulate the structure and properties of materials by doping with non-precious metal elements. It should be noted that the reproducibility of the doping process, cost-effectiveness, and feasibility of large-scale production are still issues of concern for industrial applications.

In short, the incorporation of various heteroatoms such as transition metals and non-metal elements into manganese oxides not only effectively improves the level of conductivity and modulates the surface properties, but also generates additional active sites for the ORR and OER, thereby enhancing the electrocatalytic performance. In the chemical process of preparing heteroatom-doped MnO_2, doping with metal cations proved to be more facile and efficient. This is mainly due to the good compatibility of the metal cations with the MnO_2 structure, which allows the doping process to proceed smoothly. Specifically, to realize the doping of metal cations, we usually adopt a simple and direct method: adding the appropriate amount of cationic salt directly to the MnO_2 precursor solution. However, the conditions for doping non-metal anions are more stringent and often require high temperatures, special channels, and strict conditions. Moreover, the addition of dopants may affect the lattice structure and crystal size of MnO_2, and thus affect its stability. In addition, adding dopants may increase the complexity and cost of the synthesis process. Therefore, when selecting and adding dopants, it is necessary to carefully study their potential effects on the electrochemical performance and stability of manganese dioxide, and optimize and improve them in practice.

2.4 Manganese dioxide composite material

As a common strategy for making better function materials, the formation of compositions can combine the merits of the composited substance, as well as cause the so-called "synergy effect" near the compositing interface. The following part will summarize the compositing strategy to construct advanced bifunctional MnO_2 by the substance of the composites.

2.4.1 With carbon material. Carbon-based nanomaterials (in particular heteroatom-modified carbon materials with electroneutrality breaking and charge repositioning) are considered to be very promising electrochemical materials because of their low price, high specific surface area, good electrical conductivity, chemical stability and ease of processing. Recently, the compositing of MnO_2 onto carbon-based materials with a large specific surface area and high conductivity (*e.g.*, carbon black,[99] carbon flake paper, graphene,[100] carbon nanofibers,[101] carbon nanotubes,[102] mesoporous carbon,[103] carbon nitride,[104] *etc.*) has been extensively investigated. What's more, it is widely reported that nanocarbon materials can also effectively disperse MnO_2 nanocrystals, prevent them from agglomerating and ensure that they are distributed more evenly. Because of this, the catalyst is more durable and the dispersed nanocrystals have an increased accessible surface area to react more efficiently with the reactants, which further improves the catalytic performance.[105] Benefiting from the above merits, the manganese dioxide/carbon composites as electrode materials can highly improve the battery performance of zinc–air batteries.[106]

2.4.1.1 ORR performance. Graphene and carbon nanotubes, two of the representative carbonaceous materials, have great potential in improving the ORR efficiency of MnO_2, which is attributed to their large surface area, excellent conductivity characteristics and abundant available resources. Chen *et al.* first directly synthesized reduced graphene oxide on stainless steel fiber felt (SSFF) and then deposited MnO_2 *in situ* on an rGO-SSFF conducting support electrode (denoted as rGO@MnO_2-SSFF) as shown in Fig. 12a.[97] The test results show that the ORR capability of the rGO@MnO_2-SSFF material is larger than that of the Pt/C-carbon cloth (Pt/C-CC) (Fig. 12b). This outstanding performance can be attributed to the 3D porous structure of the conductive substrate, which enables the preparation of a cathode with a larger electrochemically active area than that of the Pt/C-CC cathode. Because of that, the rGO@MnO_2-SSFF-24 cathode (with a deposition time of 24 h) has more active sites, leading to greater catalytic capacity. The proposed method of *in situ* deposition of MnO_2 nano-catalysts avoids the need for binders and additional fabrication steps required in the preparation of conventional powder catalysts, which not only saves cost in terms of materials and energy but also ensures high electrical output of microbial fuel cells. However, further research should aim at improving the long-term stability of the material, delving into its reaction mechanism, and investigating its feasibility in zinc–air batteries.

Munaiah *et al.* have successfully prepared MnO_2 blended multi-walled carbon nanotube (MWCNT) nanocomposite materials (MnO_2/MWCNT) employing a simple wet chemical method illustrated in Fig. 12c.[98] The layered MWCNT wrapped around MnO_2 formed a 3D hollow porous network structure, which ensured the complete permeability and wettability of the electrolyte. In addition, the MWCNT-modified MnO_2 enhanced the electronic conductivity by improving the inter-particle contact which is favorable for the oxygen reduction performance. Because of the embedding and de-embedding of Na^+ in
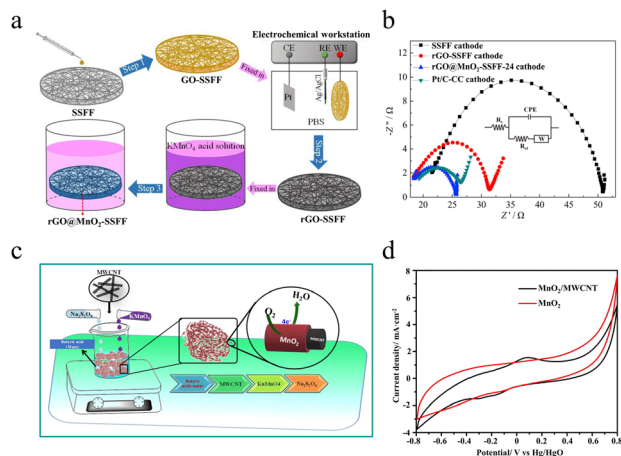
29370 | *J. Mater. Chem. A*, 2024, **12**, 29355–29382

This journal is © The Royal Society of Chemistry 2024

Fig. 12 The preparation method and ORR performance of rGO@MnO$_2$-SSFF and MnO$_2$/MWCNT. (a) Synthesis procedures of rGO@MnO$_2$-SSFF. (b) EIS curves of the SSFF cathode, rGO-SSFF cathode, rGO@MnO$_2$-SSFF-24 cathode and Pt/C-CC cathode. Reproduced with permission.[97] Copyright 2021, Elsevier. (c) The schematic illustration of MnO$_2$/MWCNT nanocomposite preparation. (d) CV curves of MnO$_2$/MWCNT and hollow structure of MnO$_2$ in N$_2$ purged 0.05 M Na$_2$SO$_3$ + 0.1 M NaOH solution at a scan rate of a modified glassy carbon electrode (GCE). Reproduced with permission.[98] Copyright 2019, Elsevier.

the obtained MnO$_2$/MWCNT electrode, the composite exhibits typical redox behavior (Fig. 12d). But this phenomenon does not occur on the pure MnO$_2$ electrode. This highly redox-active MnO$_2$/MWCNT electrode significantly enhances the ORR kinetics through a four-electron pathway mechanism, and the MnO$_2$/MWCNT composite exhibits superior ORR selectivity as compared to the benchmark Pt/C electrocatalysts in the presence of methanol. As a whole, the prepared MnO$_2$/MWCNT composite electrocatalyst demonstrates excellent catalytic

performance and methanol tolerance in the ORR. This study highlights the key role of the synergistic interaction between different components in the composite to improve the overall performance.

2.4.1.2 OER performance. In recent years, carbon dots (CDs) have been used as effective electrocatalysts for various types of reactions owing to their high electrical conductivity, low cost, simple synthesis method, low toxicity, and good electron transfer ability. In addition, carbon dots with rich functional groups (*e.g.*, –OH, – COOH, and –NH$_2$) on their surfaces can also provide many useful sites for the fabrication of electrochemical catalysts. Tian and colleagues have reported a novel class of CDs (carbon dots)-MnO$_2$ synthesized by a facile microwave-assisted hydrothermal approach (Fig. 13a).[107] By adding CDs, the large MnO$_2$ nanoflowers can split into several tiny nanoflowers with slightly rougher surfaces. This prepared CDs-MnO$_2$ not only possesses a higher specific surface area, better conductivity, and a more rapid charge transfer pathway but also exhibits significantly enhanced electrocatalytic activity. What's more, it avoids the phenomenon of agglomeration and corrosion of the catalyst in alkaline environments, thus greatly improving the stability of the catalyst. Remarkably, as seen in Fig. 13b and c, the CDs-MnO$_2$ shows higher performance for the OER than the pure MnO$_2$ sample, with a relatively low Tafel slope (43.6 mV dec^{-1}), a small overpotential, and high electrocatalytic and structural stability. Beyond that, carbon materials doped with non-metal elements such as nitrogen, boron, and sulfur are worth considering as support materials with improved conductivity and enhanced stability. Overall, this study successfully constructed a new class of highly efficient OER catalysts through a simple preparation method, large-scale production of carbon dots and their compounding with non-precious metal catalysts. This finding is not only important in reducing catalyst costs but
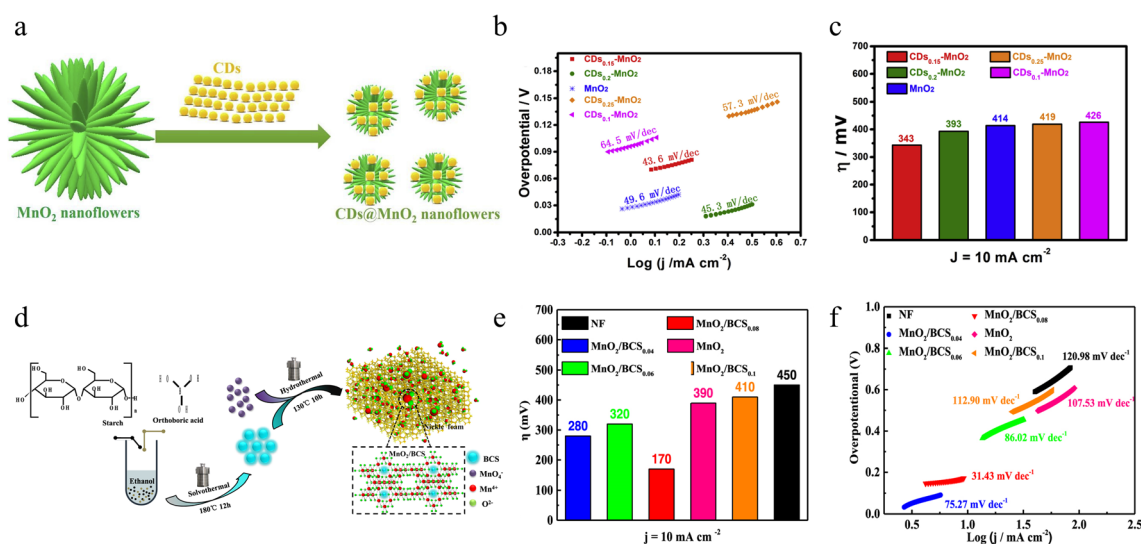

Fig. 13 The preparation method and OER performance of CDs–MnO$_2$ and MnO$_2$/BCS. (a) Synthetic illustration of CDs–MnO$_2$. (b) Tafel slopes and (c) Overpotentials of different CDs–MnO$_2$. Reproduced with permission.[107] Copyright 2019, Elsevier. (d) Synthetic illustration of BCS and the derived MnO$_2$/BCS composites. (e) Histogram of the obtained overpotentials of MnO$_2$/BCS$_{0.04}$, MnO$_2$/BCS$_{0.06}$, MnO$_2$/BCS$_{0.08}$, MnO$_2$/BCS$_{0.1}$ and pristine MnO$_2$. (f) Tafel plots. Reproduced with permission.[108] Copyright 2022, IOP.

This journal is © The Royal Society of Chemistry 2024

J. Mater. Chem. A, 2024, **12**, 29355–29382 | **29371**

also provides a new way to develop more economical and sustainable catalyst materials.

Dong *et al.* successfully fabricated a novel type of boron-doped carbon sphere (BCS) as well as a derived MnO_2 nano-electrocatalyst (MnO_2/BCS) by a simple one-step hydrothermal route (Fig. 13d).[108] Compared to other samples, the MnO_2/BCS nanoflowers consist of many nanosheets that have smaller particle sizes, eventually leading to a higher specific surface area. Owing to the excellent characteristics of BCS, including high electrical conductivity, strong electron transfer capability and large specific surface area, MnO_2/BCS nanocomposites prepared with various BCS additions have significantly higher electrocatalytic OER efficiency than the pure MnO_2. The results of electrochemical tests show that the MnO_2/BCS$_{0.08}$ (the content of BCS is 0.08 g) electrocatalyst achieves a lower over-potential than that of other samples and faster reaction kinetics with a minimum Tafel slope value of only 31.43 mV dec^{-1}, which is comparable to that reported for RuO_2 (Fig. 13e and f). In general, this study successfully designed and synthesized a novel MnO_2/BCS composite electrocatalyst, which demonstrated an excellent catalytic effect in terms of OER performance. The catalyst is not only cost-effective and has superior performance, but also demonstrates good long-term stability, which is promising for a wide range of applications. However, future studies should deeply explore its mechanism of action, optimize the synthesis process and comprehensively evaluate its performance under different conditions to promote the practical application of this catalyst in the energy field.

2.4.1.3 ORR & OER performance in a zinc–air battery. As is well known, MnO_2 composites with carbon materials play a significant role in the ORR and OER, enhancing the overall performance and efficiency of electrochemical processes. Xu *et al.* cleverly utilized a facile two-step hydrothermal reaction approach to successfully prepare a unique bifunctional composite catalyst, which is composed of interwoven hormone-like MnO_2 and CNTs (MnO_2/CNTs).[109] This hybrid catalyst exhibits an exquisite morphology similar to that of hortensia, and its high-density reaction surface significantly enhances the contact probability with O_2 and OH^- ions. The design of a high specific surface area not only provides a rich three-phase reaction area for the reaction, effectively promoting the adsorption/desorption process of reactants and products, but also brings about a synergistic effect between each component and the interconnected conductive network as well as greatly accelerating electron transfer, significantly improving the overall conductivity, thereby effectively preventing the occurrence of unfavorable phenomena such as structural transformation, collapse and aggregation. The testing results show that the MnO_2/CNT electrode displays significant bifunctional activity with higher reaction activity and rate, and a small potential difference of 0.85 V (Fig. 14a). The zinc–air batteries (ZABs) with MnO_2/CNTs possess a high 243 mW cm^{-2} power density and ideal durability, as seen in Fig. 14b. It's worth noting that the rechargeable ZAB exhibits remarkable cycle stability, operating for up to 500 hours as shown in Fig. 14c. Generally, the simplified preparation process helps to reduce the production cost and increase the output efficiency of the material. With

unique structural advantages and remarkable electrocatalytic properties, this material has the potential to replace traditional noble metal catalysts and be used in metal–air batteries. Future research could further explore the specific mechanisms through theoretical calculations and in-depth experimental analyses to better understand and improve the properties of this composite.

Miao *et al.* successfully prepared MnO_2 nanowires by an efficient and simple one-pot method.[110] These nanowires are cleverly loaded on N-doped reduced graphene oxide (MnO_2/NRGO-urea), which provides strong support for the optimization of material properties. The core formation and growth process of MnO_2 nanowires on NRGO is particularly critical in the preparation process. This process not only realizes tight binding between the nanowires and the substrate but also promotes the formation of Mn–N–C or Mn–O–C bonds. The formation of these covalent bonds significantly enhances the electrical conductivity of the MnO_2 nanowires, enabling them to exhibit superior electrochemical performance. In addition, these nanowires exhibit a thin and long morphology with a large specific surface area. This unique structure not only provides more channels for electron and ion transport but also greatly increases the density of active sites. As Fig. 14d shows, MnO_2/NRGO-urea exhibits excellent bifunctional properties, such as larger $E_{1/2}$ of the ORR, lower overpotential of the OER, and the ΔE is 0.89 V at 10 mA cm^{-2}, compared to other samples in this work. Moreover, all-solid-state flexible ZABs using MnO_2/NRGO-urea as a cathode demonstrate small charge/discharge potential gaps and long-term stable cycling performance as depicted in Fig. 14e and f. In conclusion, the energy conversion efficiency and power density of the cells are significantly improved by designing an efficient MnO_2/NRGO-urea catalyst and a PAM-based electrolyte with high conductivity. This provides a solid technical foundation for the application of all-solid-state ZABs in flexible electronic devices and promotes the further development of this field.

Despite conventional carbon materials, biomass carbon materials are also one of the promising conductive substances owing to their renewability and environmental friendliness.[112,113] For instance, shrimp shells, a natural material rich in unique ingredients such as protein and chitin, have been regarded as a highly promising N-doped porous carbon precursor. Through careful processing and transformation, shrimp shells can be used in the field of electrochemical energy storage, showing unique advantages and broad application prospects.[114] Xiao *et al.* chose shrimp shells as a carbon source and calcined them to form a porous carbon skeleton. Subsequently, they studied the *in situ* redox reaction method to prepare an ultrathin amorphous MnO_2-modified prawn shell-derived porous carbon composite.[111] The prepared composites possess the advantages of both amorphous MnO_2 and shell-derived porous carbon, such as abundant defects and catalytically active sites, enhanced electronic conductivity, and good gas diffusion pathways. Moreover, the strong interaction between MnO_2 and carbon materials offers the possibility of efficient bifunctional properties. As shown in Fig. 14g, the composite material prepared with 0.01 mol per L $KMnO_4$
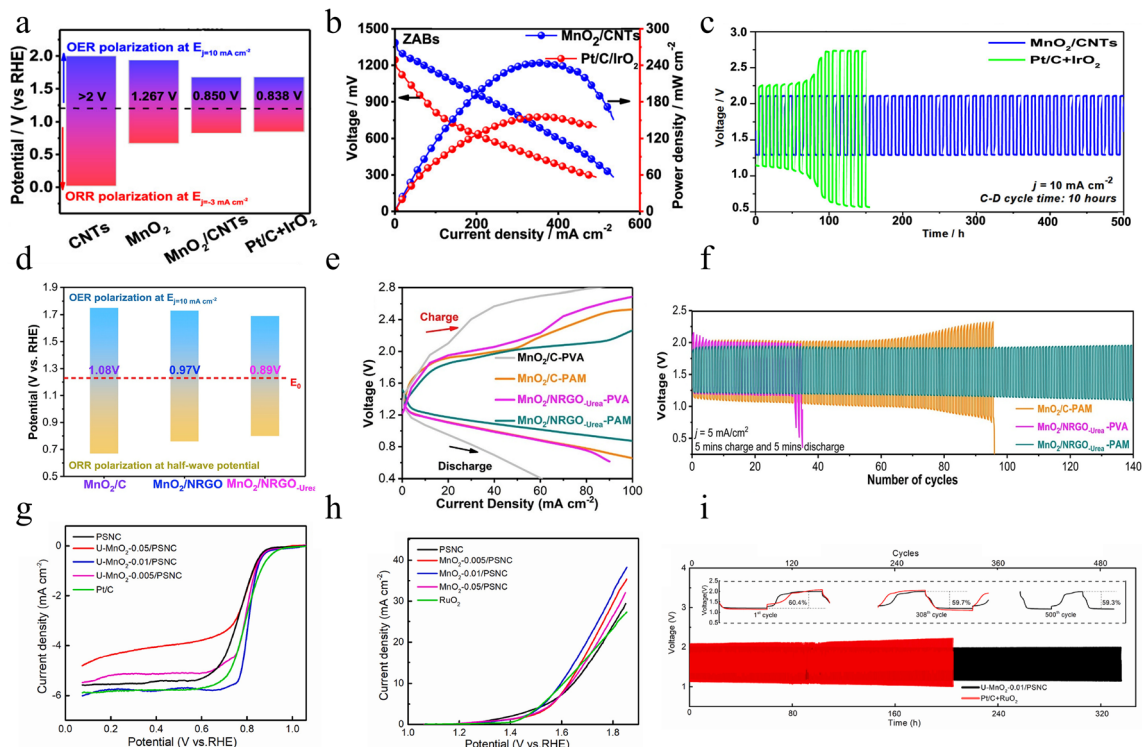
29372 | *J. Mater. Chem. A*, 2024, **12**, 29355–29382

This journal is © The Royal Society of Chemistry 2024

Fig. 14 The electrocatalytic performance of MnO_2 composites with carbon materials. (a) Comparison of the ΔE between MnO_2/CNTs prepared by a two-step hydrothermal method and other samples. (b) Discharge and power density curves. (c) Charge–discharge cycling curves of the rechargeable ZABs. Reproduced with permission.[109] Copyright 2019, American Chemical Society. (d) ΔE of MnO_2/NRGO-urea prepared by the one-pot method and Pt/C. (e) Charge–discharge polarization curves. (f) Charge–discharge cycling curves. Reproduced with permission.[110] Copyright 2020, Elsevier. (g) LSV curves for the ORR, (h) LSV curves for the OER, and (i) long-term cycling test plot of U−MnO_2-0.01/PSNC prepared by a redox reaction method and benchmark catalysts. Reproduced with permission.[111] Copyright 2022, Elsevier.

(denoted as U−MnO_2-0.01/PSNC) possesses a more positive half-wave potential and better diffusion-limited current density than the benchmark catalyst, demonstrating superior ORR performance. Moreover, Fig. 14h shows that the U−MnO_2-0.01/PSNC exhibits excellent OER performance, such as a smaller overpotential which is slightly superior to that of the commercial RuO_2 and displays a minimal ΔE, and even outperforms many other carbon-based catalysts.[115–118] Besides, the U−MnO_2-0.01/PSNC based RZAB exhibits good cycling characteristics with a small increase of discharge–charge gap (0.01 V) for 334 h as depicted in Fig. 14i. However, it should be noted that biomass carbon materials also have some challenges, such as the stability of raw material supply, the complexity of the preparation process and the controllability of the product properties, which need to be solved by further research and development. In conclusion, this study provides new ideas and methods for the development of low-cost and high-performance catalysts for metal–air batteries and lays the foundation for their future promotion in commercial applications.

In other words, manganese dioxide has been compounded with a variety of engineered carbon materials, including carbon nanotubes, sulfur and/or nitrogen-doped carbon nanosheets, and porous carbon nanoparticles. Compared with bare MnO_2, the manganese dioxide composites with carbon not only enhance conductivity but also provide more additional active sites, as well as effectively preventing structural collapse/agglomeration. Since the efficiency of improving conductivity and electrocatalytic activity depends on the degree of electronic coupling between the complex species, it is necessary to maximize the interfacial interactions between the manganese dioxide and the conducting carbon materials. It is important to elucidate the chemical connectivity of the composite components and the interactions that collaborate to enhance the material properties. However, carbon materials are prone to oxidation and corrosion due to reactive oxygen species during the OER process, which can lead to reduced efficiency of cathode catalysts and decreased battery performance. In summary, although carbon/manganese dioxide composites have the advantages of high activity and high efficiency, there are still some shortcomings in the catalytic process, which need to be further studied and improved.

2.4.2 With other metals/metal oxides. In addition to what has been mentioned above, MnO_2/metal and MnO_2/metal oxide composites are also superior bifunctional catalytic materials that display promising applications in ZABs. MnO_2 can be compounded with many metals and metal oxides (*e.g.*, Fe,[119] Co, Ni,[120] Ag,[121] Co_3O_4,[122] Fe_2O_3,[123] PbO_2,[124] La_2O_3,[125] *etc.*). These composites usually exhibit fast electron transportation and thus show improved electrocatalytic performance.

This journal is © The Royal Society of Chemistry 2024

J. Mater. Chem. A, 2024, 12, 29355–29382 | 29373

2.4.2.1 ORR performance. The amorphous/crystalline heterostructure can deliver more active sites and modulate the electronic distribution, thus optimizing the oxygen species adsorption energy and improving the electrocatalytic performance for the ORR and OER. Wang *et al.* first synthesized amorphous MnO_2 with oxygen vacancies by a chemical redox method and then used a wet chemical strategy to form ultrafine, well-dispersed Pd nanoparticles on the surface of amorphous MnO_2 nanosheets (Pd/a-MnO_2).[126] The flexible amorphous substrate is more conducive to the migration of electrons and can further strengthen the interaction between the metal and carrier. The synergistic interaction between Pd and amorphous MnO_2 greatly improves ORR catalytic activity in alkaline environments. Amorphous MnO_2 (a-MnO_2) is rich in defect sites and unsaturated coordination sites, enabling it to effectively stabilize Pd nanoparticles and avoid their agglomeration. Pd/a-MnO_2 has more Mn^{3+} species and oxygen vacancies in comparison with the crystal counterpart (Pd/c-MnO_2). It is known that oxygen vacancies can promote the adsorption of oxygen molecules, which is favorable for the breaking of O–O bonds and accelerates the ORR kinetics. The co-interaction between Pd and amorphous MnO_2 leads to a downward shift of the d-band center, facilitating the desorption of the key intermediate *OH in the ORR process and greatly improving the catalytic performance. As described in Fig. 15a–d, the optimized Pd/a-MnO_2 exhibits superior ORR performance in comparison to that of the benchmark catalyst, with more positive $E_{1/2}$, faster reaction kinetics, maximum mass activity and outstanding stability. In this study, the relationship between the structure and performance of Pd and amorphous MnO_2 has been deeply revealed through interface engineering design. This structure-to-property exploration provides theoretical support and guidance for the design of more efficient electrocatalysts, which can contribute to the improvement and application of future catalysts and be extended to other metal and amorphous metal oxide carriers.

Yang *et al.* successfully synthesized nanosheet-assembled MnO_2 micro-flowers decorated with multiple hollow CeO_2 spheres (CeO_2/MnO_2) as an oxygen electrocatalyst for the ORR by a two-step hydrothermal approach.[127] The CeO_2/MnO_2 composite with a unique structure catalyst exhibits highly efficient ORR electrocatalytic activity compared to floral MnO_2 and hollow CeO_2 sphere monomers, which is ascribed to the co-effect between the hollow CeO_2 and hierarchical nanosheet-assembled MnO_2. As shown in Fig. 15e, The CeO_2/MnO_2 electrode displays higher E_{onset} and larger $E_{half-wave}$ than that of either of the CeO_2 and MnO_2 electrodes. What's more, the number of electrons transferred is approximately 4.0, demonstrating good reaction kinetics (Fig. 15f). These superior properties make CeO_2/MnO_2 composites have the potential to be candidates for cathode catalysts in the field of metal–air batteries. Meanwhile, this study provides new ideas and insights for further exploring the application of MnO_2 and other metal oxide composite structures in electrocatalysis.

2.4.2.2 OER performance. Xu *et al.* have successfully reported a simple electrostatic approach to prepare gold-decorated 2D δ-MnO_2 nanosheet composites (Au-MnO_2) with different gold loading ratios.[128] Under low-power irradiation with 200 mW green laser light, the composites show superior OER catalytic properties. The electrochemical results indicated that the OER catalytic performance could be significantly improved by activating the localized surface plasmon resonance of gold nanospheres under 532 nm laser irradiation. By regulating the laser intensity from 100 mW to 200 mW, the obtained Au-MnO_2-200
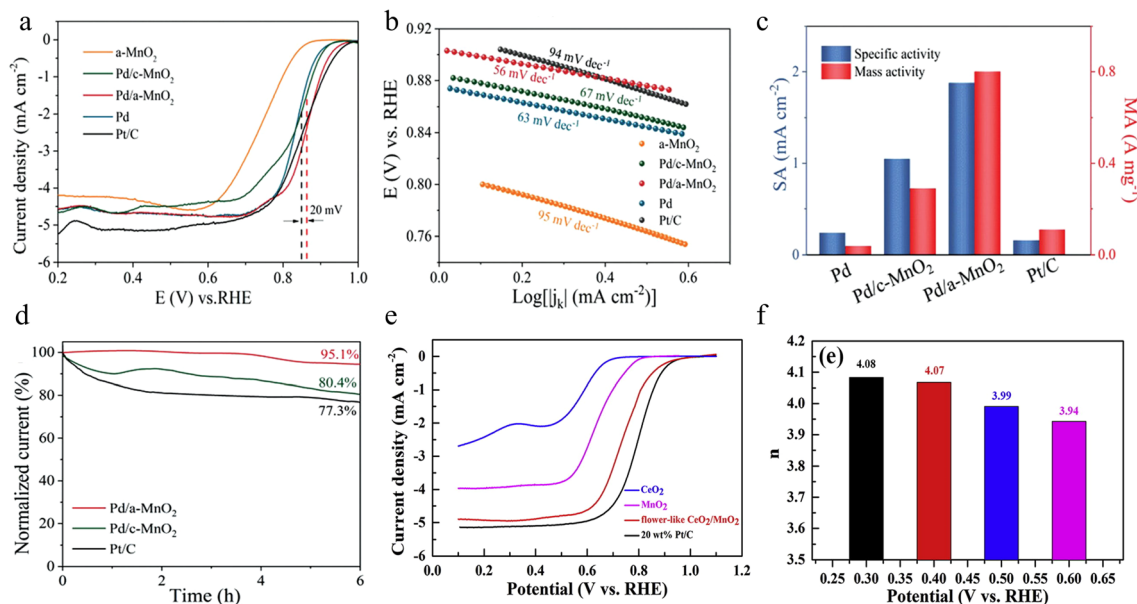

Fig. 15 The ORR performance of Pd/MnO_2 and CeO_2/MnO_2. (a) LSV curves of samples. (b) Tafel plots for the ORR. (c) Mass and specific activities of catalysts toward the ORR at 0.85 V. (d) Current−time chronoamperometric response for Pd/a-MnO_2, Pd/c-MnO_2, and Pt/C at 0.75 V. Reproduced with permission.[126] Copyright 2023, Wiley-VCH. (e) LSV curves of different samples and commercial 20 wt% Pt/C. (f) Calculated electron transfer number of the composite at different potentials. Reproduced with permission.[127] Copyright 2019, Elsevier.

29374 | *J. Mater. Chem. A*, 2024, **12**, 29355–29382

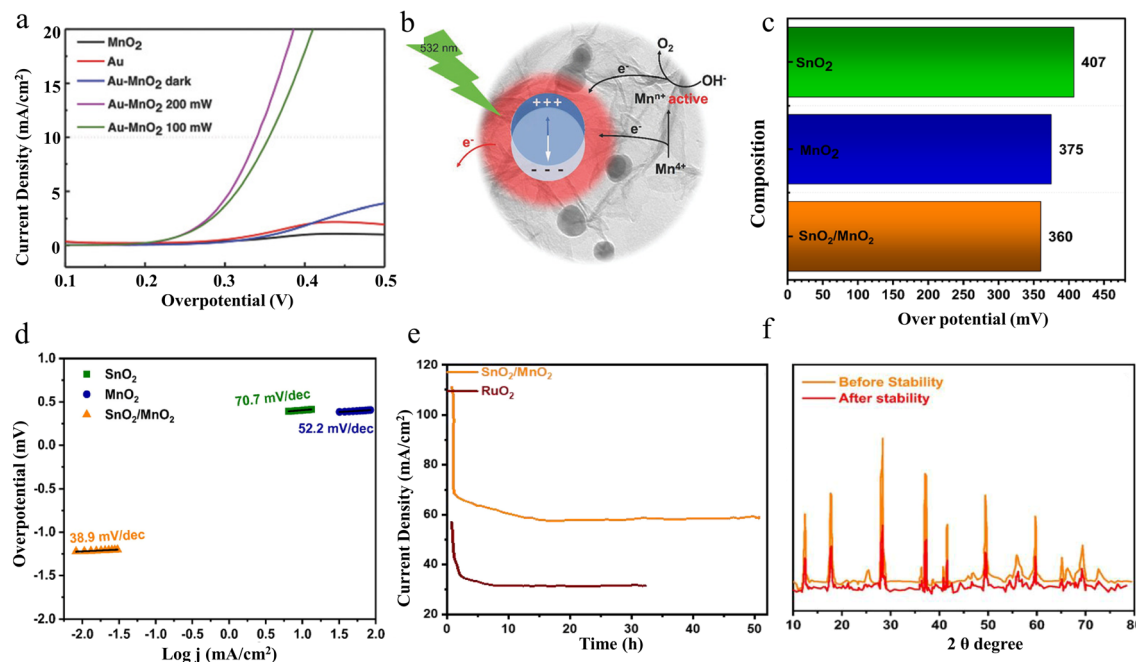This journal is © The Royal Society of Chemistry 2024

Fig. 16 The OER performance of Au–MnO₂ and SnO₂/MnO₂. (a) OER polarization curves of different samples. (b) Schematic electron transfer path that possibly occurs in the Au-MnO₂ nanocomposites under 532 nm laser irradiation. Reproduced with permission.[128] Copyright 2018, Wiley-VCH. (c) η and (d) LSV of SnO₂, MnO₂ and SnO₂/MnO₂. (e) chronoamperometry. (f) XRD stability of SnO₂/MnO₂. Reproduced with permission.[129] Copyright 2023, Elsevier.

sample shows the lowest overpotential, which is comparable to that of recognized good OER catalysts (Fig. 16a). In addition, plasma-induced hot electron excitation can be used as an available electron trap to restrict the Mn^{4+} outer electrons, resulting in the creation of electron-confined active Mn^{n+} entities. As seen in Fig. 16b, the obtained active Mn^{n+} species can provide reaction sites for electron transfer from electrolytes, facilitating the formation of OOH intermediates and subsequent deprotonation, ultimately leading to efficient OER performance. In this study, Au-decorated 2D δ-MnO₂ nanosheet composites are successfully prepared and efficient OER catalytic performance under low-power green laser irradiation is achieved by the laser-activated localized surface plasmon resonance effect of gold nanorods. The study reveals the intrinsic mechanism of plasma-induced hot-electron excitation for the enhancement of catalytic performance, which provides a new direction for photoelectrochemical synergistic catalysis.

Alwadai *et al.* employed a simple one-step hydrothermal method to prepare SnO₂/MnO₂ nanocomposites.[129] The nanocomposites prepared by vertically aligned irregularly shaped nano-cubic SnO₂ and MnO₂ nanorods joined together to form hierarchical nanostructures exhibit enhanced catalytic performance primarily due to their impressive electrochemical surface area (49.69 m² g⁻¹). As Fig. 16c and d show, SnO₂/MnO₂ electrocatalysts exhibit strong OER activity with a low overpotential of 360 mV and a Tafel slope value of 38.9 mV dec⁻¹. In addition, the MnO₂/SnO₂ nanocomposites exhibit significantly better stability than that of the reference RuO₂ over 45 hours (Fig. 16e and f). They are among the currently competitive and efficient OER catalysts due to the simple synthesis method,

good catalytic effect and high stability. This study raises the possibility of further constructing binary or ternary nanocomposites by electrochemical oxidative restructuring of the morphology and surfaces and introducing other counterparts or material substitutions. This concept provides a new idea for the design of efficient catalysts in the future, which is expected to achieve more efficient and stable electrocatalytic performance through rational design and a combination of different materials.

2.4.2.3 ORR & OER performance in a zinc–air battery. In general, manganese dioxide compounded with metals or metal oxides can form more complex structures and interfaces, thus providing more reactive active sites and increasing the reaction rate. Not only that, the surface properties and structure of the material can be modulated. By optimizing the surface properties of the material, we can improve its interaction with the reactants and thus enhance the catalytic performance. At the same time, adjusting the structure of the material can ensure its higher stability and durability during the catalytic process.

Compared with the only single-metal composite, the manganese dioxide composite with multiple metals has more active sites and better stability, which can enhance catalytic efficiency and reduce energy consumption. Wang *et al.* reported a high-efficiency and low-cost Janus MnO₂–NiFe composite by a simple two-step electrodeposition technology.[130] The Janus MnO₂–NiFe/Ni electrode separating the OER and ORR activity can prevent the oxidation of MnO₂ and the devastation of the gas diffusion layer. This design not only improves the electrochemical performance of the electrode but also enhances the stability and durability of the electrode. The MnO₂–NiFe

This journal is © The Royal Society of Chemistry 2024

J. Mater. Chem. A, 2024, **12**, 29355–29382 | **29375**

electrodes show favorable multiplier performance toward the ORR as indicated in Fig. 17a. The Janus MnO_2–NiFe catalyst demonstrates a small overpotential and ΔE value, indicating excellent OER and bifunctional performance as shown in Fig. 17b. Particularly, the zinc–air battery consisting of a Janus MnO_2–NiFe electrode displays outstanding electrochemical test results with excellent rechargeable stability even at high current densities, which is far superior to that of MnO_2 and the majority of electrocatalysts that have been studied (Fig. 17c). The Vaseline-assisted electrodeposition strategy proposed in the study is not only limited to MnO_2–NiFe electrodes but can also be extended for the design of Janus electrodes for other types of high-performance metal–air batteries. The innovative design of the Janus structure has led to a significant increase in the catalytic bifunctionality of the electrode material for both the ORR and OER and at the same time, it has demonstrated excellent stability. Although the Janus structure effectively enhances the catalytic performance, surface modification or

structural optimization may further enhance its performance. For example, pulsed electricity is used instead of direct current to prepare high-quality, complex films.[133]

In addition to the above, metal oxides are also effective materials that can activate MnO_2 and lead to good bifunctional catalytic activity towards oxygen reactions. For example, Hong *et al.* firstly through a spray pyrolysis method prepared a 3D CNT microsphere and then co-deposited MnO_2 and Fe_2O_3 nanorods on it by following bottom-up processes.[131] The three-dimensional porous structure of materials facilitates electron transport and mass transfer. Moreover, the agglomeration of MnO_2 and Fe_2O_3 is successfully prevented by the method of preparation described above. The reduction of agglomeration can retain more active sites, which enhances the electrocatalytic performance of MnO_2–Fe_2O_3/CNT. In terms of ORR performance, MnO_2–Fe_2O_3/CNT exhibits satisfactory testing results, such as a large onset potential and high half-wave potential, and the diffusion-limited current density of MnO_2–Fe_2O_3/CNT is
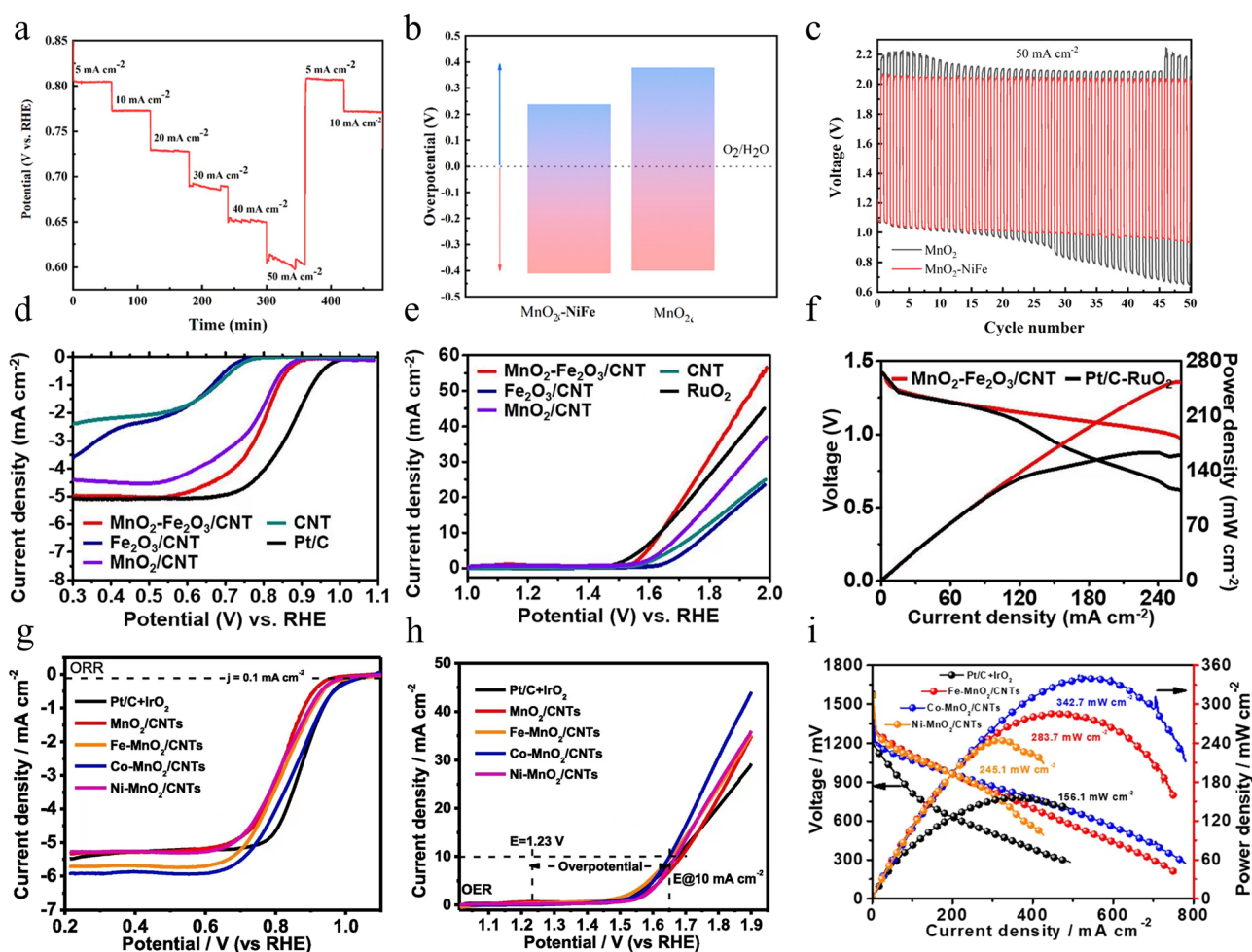

Fig. 17 The electrocatalytic performance of MnO_2 composites with metal/metal oxide materials. (a) Multitemporal potential curves of MnO_2–NiFe prepared by a two-step electrodeposition method. (b) Chrono-potential plots at the current of 20 mA cm^{-2}. (c) Stability test for MnO_2–NiFe and MnO_2 at the current of 50 mA cm^{-2}. Reproduced with permission.[130] Copyright 2019, American Chemical Society. (d) LSV curves for the ORR, (e) LSV curves for the OER, and (f) polarization curves and power density plots of MnO_2–Fe_2O_3/CNT prepared by spray pyrolysis and a subsequent bottom-up method and other samples. Reproduced with permission.[131] Copyright 2021, Elsevier. (g) ORR polarization curves, (h) OER polarization curves, and (i) the discharging polarization curves and power density plots for M–MnO_2/CNTs (M: Fe, Co and Ni) prepared by a hydrothermal method and other samples. Reproduced with permission.[132] Copyright 2020, Elsevier.

29376 | *J. Mater. Chem. A*, 2024, **12**, 29355–29382

This journal is © The Royal Society of Chemistry 2024

similar to that of Pt/C, demonstrating excellent electrocatalytic activity for the ORR (Fig. 17d). In terms of OER performance, MnO_2–Fe_2O_3/CNT exhibits a low overpotential as good as RuO_2 (Fig. 17e). Especially, the Zn air battery with MnO_2–Fe_2O_3/CNT shows a maximum power density of 253 mW cm^{-2}, which is higher than that of Pt/C–RuO_2 (Fig. 17f). The charge–discharge potential difference of MnO_2–Fe_2O_3/CNT-based zinc–air batteries only increases a little after 3500 min of charge–discharge cycling. The 3D porous structure of the composite and the large number of active sites from the co-deposition of nanorods significantly enhanced the catalytic performance. This synthetic strategy of 3D structures consisting of CNTs and metal oxides can be used to develop efficient hybrid electrocatalysts for ZABs.

Xu *et al.* first prepared MnO_2 by a simple hydrothermal method and then used the obtained MnO_2 to react with carbon nanotubes and metal nitrates in an alkaline solution at 160 °C for six hours, followed by calcining the resulting samples in a furnace (350 °C for 1 h), finally obtaining metal oxide (MO_x, M = Fe, Co, and Ni) anchoring MnO_2/CNTs hybrid catalysts with a unique hierarchical structure (M–MnO_2/CNTs).[132] Generally "heteroatom-doped MnO_2" means a uniform doping of heteroatoms (including both metal and non-metal atoms) into the whole catalyst, while "metal-anchoring" emphasizes the doping of metal atoms onto the surface, which function as "linkers" in the form of metal–O bonds. Compared with MnO_2/CNTs and reference catalysts, M–MnO_2/CNTs (M = Fe, Co, Ni) exhibit impressive catalytic activity, especially in the ORR and OER. When transition metal elements such as Fe, Co, Ni, *etc.* are introduced into MnO_2, strong interactions occur between these metals and MnO_2. This interaction not only changes the electronic state of the Mn but also affects the distribution of the electron cloud around it. As a result, these redistributed electrons can more efficiently interact with reactants during the ORR and OER processes, thus facilitating the reactions. The unique hierarchical structure improves mass transfer and builds a high-speed electron transfer network through composite carbon nanotubes. Co–MnO_2/CNTs have a higher onset potential and limiting current density during the ORR process (Fig. 17g). Besides, M–MnO_2/CNTs also exhibit high electrocatalytic performance with a lower overpotential in the OER (Fig. 17h). Moreover, Co–MnO_2/CNTs exhibit a lower ΔE value compared to that of Fe–MnO_2/CNTs and Ni–MnO_2/CNTs. Furthermore, as shown in Fig. 17i, the Co–MnO_2/CNTs catalyst used in zinc–air batteries displays good electrochemical properties, reaching the highest power density of 342.7 mW cm^{-2}. Not only that, Co–MnO_2/CNTs-based zinc–air batteries exhibit better cycling stability relative to other M–MnO_2/CNTs, capable of stable cycling for 129 h. In other words, this study introduced aminated carbon nanotubes (CNTs-NH_2) as a hierarchical hybridised substrate, which can significantly enhance the electron transport capacity of M–MnO_2, and thus the catalytic performance of the overall composites. This study compares the catalytic performance of the composite with different oxides as cathodes for zinc–air batteries. Meanwhile, the excellent battery performance demonstrated by M–MnO_2/CNTs highlights its

potential application in large-scale zinc–air batteries such as high-energy electric vehicles and stationary energy stations.

In short, the synergy between manganese dioxide and the composited component usually leads to better stability and electrocatalytic activity of the cathode. With the compositing of a carbonaceous material, the overall cost can be reduced; the conductivity can be improved; there will be a greater chance for breaking the scaling effect between the OER/ORR due to the p–d band interaction;[95] and the various morphologies and ease of synthesis offer considerable room for activity tuning. However, carbonaceous materials possess poor stability under alkaline and strongly oxidative conditions. Furthermore, benefiting from the strong d–d band interaction, the use of MnO_2 with metal/metal oxide composites in the cathode also improves the charge transfer process, reduces the polarization of the cathode, increases the specific capacitance, and enhances the overall energy density of the cell. The incorporation of metal/metal oxide nanoparticles in the cathode may also result in the formation of a porous architecture, which provides a large surface area, facilitating the diffusion of mass. However, the stability of metals is also not very good; metal oxides are usually less conductive than carbon. In summary, the development of composite cathodes for Zn–air batteries is a promising way to conquer the limitations of traditional cathode materials. The use of manganese dioxide in combination with metals/metal oxides has been shown to be an effective approach to enhancing the performance of Zn–air batteries, leading to improved energy efficiency, stability, and durability. However, the synthesis of complexes is complex, which increases the difficulty and cost of industrial production, and many factors in the preparation process may affect the performance and it is difficult to achieve the perfect theoretical value. Therefore, when selecting composites, it is necessary to evaluate and comprehensively consider them according to specific application scenarios and select more suitable composite materials.

3 Summary and outlook

The sluggish rates of the ORR and OER on the cathode of RZABs hinder their large-scale application. The bifunctional performance can be optimized by studying efficient, durable and economical electrocatalysts. As is well known, due to the low price, abundant resources, and environmental friendliness, transition-metal compound (TMC) catalysts represent a class of potential substituted catalysts that are used to defeat the catalyst challenges related to expensive Pt and RuO_2. In particular, MnO_2-based materials have received great attention as excellent electrocatalysts for ZABs due to their variable valence state and favorable structural and redox properties. Unfortunately, a lot of disadvantages such as low conductivity, aggregation behavior and insufficient active sites hinder their application as electrocatalysts. Therefore, the modification of the ORR and OER activity of manganese dioxide as a bifunctional electrode for ZABs by structural and morphological control, doping engineering, and composite material formation has been summarized in this review. The specific research results of the as-described bifunctional MnO_2 catalysts for ZABs are shown in

Table 1. Cycling stability in rechargeable zinc–air batteries is one of the most important indicators for their commercialization. With the increase of the number of cycles, the pure MnO_2 electrode undergoes microstructural changes, resulting in a decrease in electrode activity; polarisation occurs at the solid–liquid interface during charging and discharging, affecting the electrochemical reaction rate; and the MnO_2 electrode is prone to decomposition and detachment in environments such as those with high temperature and high pressure. Through different strategies to adjust the crystalline form, morphology and electronic structure of MnO_2, the modified MnO_2 has demonstrated significant advantages because of its stability, good electrochemical performance and efficient catalytic activity in rechargeable zinc–air batteries (RZABs), which can effectively withstand multiple cycles with less performance degradation. Its potential applications in large-scale energy storage systems, electric vehicles and emergency backup power are promising. With the continuous development of technology, the application of MnO_2 in RZABs will provide strong support for efficient and reliable energy storage solutions.

In addition to the four strategies mentioned in this paper, the fabrication of cationic vacancies and oxygen defects is also a strategy to improve the oxygen electrocatalytic activity of MnO_2. Oxygen vacancies in metal oxides can improve the catalytic performance because oxygen vacancies not only act as active sites, but also change the geometric and electronic structure as well as the chemical properties of the metal oxides. For example, the OER performance of MnO_2 can be enhanced by treating MnO_2 with a reducing agent to produce abundant oxygen vacancies and active sites,[134] and the ORR performance can be enhanced by heating MnO_2 to prepare oxides with adjustable oxygen vacancy concentrations.[135,136] In addition, the oxygen vacancies in MnO_2 can be increased by proton irradiation and doping to enhance the oxygen electrocatalytic effect.[137,138] Although these materials have shown excellent performance in a variety of electrocatalytic applications, their use as bifunctional catalysts in Zn–air batteries has been relatively less studied. This field is still in the exploratory stage and

has much untapped potential. Future research could focus more on this direction to investigate the performance of these materials in zinc–air batteries and optimize their electrocatalytic activity and stability, thereby promoting the development of zinc–air battery technology.

Generally, the four different strategies can all optimize the ORR and OER performance but with different mechanisms ranging from (I) improving the conductivity and surface area to (II) introducing p states; (III) introducing a second adsorption site; (IV) introducing a proton acceptor group; (V) the strain effect; and (VI) O–O direct coupling in the absence of *OOH, in which (I) is a general idea for electrocatalysts and (II)–(VI) refer to the mechanisms of breaking the scaling relationship.[95] From the crystal structure point of view, the crystal structure design of the ORR focuses more on the rational utilization and distribution of oxygen vacancies; the crystal structure design of the OER focuses more on the stability of reaction intermediates and the optimization of electron transport. Tuning the crystal structure to change the electrocatalytic properties of manganese dioxide is related to mechanism (I) and mechanisms (V and VI). From the viewpoint of morphology, the morphology design of the ORR often requires highly structurally controllable morphologies, such as porous structures or highly structured surfaces, to increase the adsorption of oxygen molecules and improve the diffusivity of oxygen on the surface of the catalyst, while the OER design focuses more on the generation of more active sites and the enhancement of the electron transport efficiency. Modulation of the morphology of MnO_2 to improve the catalytic activity and stability to provide better performance for electrocatalytic applications is mainly achieved through the "improving conductivity and surface area" mechanism (I) and the "strain effect" mechanism (V). From the perspective of doping, the ORR often needs doping with some elements with large electron affinity to increase the electron affinity of the active sites, to promote the adsorption and dissociation of oxygen molecules; the OER may require more the improvement of electrical conductivity and the increase of active sites, by, for instance, the doping of some elements with better electrical conductivity,

Table 1 Summary of the electrocatalytic performances of the bifunctional catalysts described in this review

Strategy	Catalysts	$E_{1/2}$ (V vs. RHE)	$E_{j=10}$ (V vs. RHE)	ΔE (V)	Stability (ORR/OER)	Ref.
Control of crystal structure	MnO_2-$IL_{0.5}$	0.83	1.624	0.794	5 h at 0.67 V/24 h at 10 mA cm^{-2}	62
	$(\alpha+\delta)$-Mn11	0.726	1.816	1.09	—	63
	ACMO	0.81	1.637	0.827	12 h at 0.57 V/60 h at 10 mA cm^{-2}	64
Control of morphology	TiC/α-MnO_2NW	0.78	1.64	0.86	—	74
	Hollow α-MnO_2	0.80	1.695	0.895	12 h at 0.57 V/24 h at 10 mA cm^{-2}	75
Heteroatom-doped manganese dioxide	CeOMS-2	0.97	1.99	1.02	—	92
	NiFeMn	0.81($E_j = -0.3$)	1.74	0.93	15 h at 0.41 V/12 h at 10 mA cm^{-2}	93
	N-MnO_2	0.797	1.639	0.842	2000 s at 0.797 V	94
Composite material with carbon material	MnO_2/CNTs	0.827	1.677	0.85	2000 cycles	109
	MnO_2/NRGO-urea	0.80	1.96	0.89	4000 s at 0.4 V/5000 s at 10 mA cm^{-2}	110
	U–MnO_2/PSNC	0.814	1.59	0.776	12 000 s at 0.814 V/12000 s at 1.59 V	111
Composite material with metal/metal oxide material	MnO_2–NiFe	0.806	1.456	0.65	24 h at 0.8 V/25 h at 20 mA cm^{-2}	130
	MnO_2–Fe_2O_3/CNT	0.80	1.63	0.83	20 000 s at 0.8 V/12 h at 10 mA cm^{-2}	131
	Co–MnO_2/CNTs	0.847	1.65	0.803	5000 cycles	132

such as Co, Ni, and so on. Doping of different elements can improve the electrocatalytic properties of MnO_2 through mechanisms (I)–(VI), but mechanism (VI) is more difficult to achieve. With respect to the composite, a composite with materials that show good ORR/OER performance or a composite with substances that can improve conductivity and stability can improve the performance of catalysts. Similarly, the electrical conductivity of the MnO_2 composites can be altered by increasing the electron migration and conduction efficiency through mechanisms (I)–(II), and the adsorption rate of reactant molecules on the surface can be increased while the reaction kinetics can be improved and the catalytic activation energy can be reduced through mechanisms (III)–(VI). It is worth noting that even if the same measure is used to optimize the material, it can produce different results depending on the method of preparation of the material.

The mechanism of each strategy is summarized as follows.

3.1 Crystal structure engineering

α-MnO_2 is well suited for use as an adsorbent material because the (2×2) tunnel structure accommodates most metal cations and water molecules. Not only is the tunnel of β-MnO_2 narrow, which is not conducive to ion diffusion, but it also has the lowest surface area and pore volume, and lower discharge capacity, making it unsuitable for use as a catalytic material.

3.2 Morphology engineering

The preparation of manganese dioxide with a high surface area provides more reaction sites and thus increases the catalytic capacity. Different morphologies also expose different crystalline surfaces, with different atomic arrangements and properties at different crystalline surfaces.

3.3 Doping engineering

Heteroatom-doping can effectively adjust the inherent characteristics of manganese dioxide, such as oxygen–manganese bond strength, crystal structure and electronic structure, thus affecting its morphology, specific surface area, oxygen vacancy formation energy and oxygen mobility. Above all, Heteroatom doping can produce synergistic effects to change the electrocatalytic properties, thereby being able to significantly improve the adsorption and catalytic properties.

3.4 Composite engineering

(1) With carbon materials: compositing with carbon materials can improve electrical conductivity and durability, as well as providing more active sites and increased reaction centers, and the composites are more likely to break the scaling effect between the ORR and OER due to p–d band interactions.

(2) With other metal/metal oxide materials: Due to the strong d–d band interactions, compounding with metal components can accelerate electron transfer, optimize the catalyst surface properties, enhance the contact between the electrolyte and electrode, and promote the diffusion of O_2.

Despite the progress mentioned above, extensive research and development are required before these materials can achieve wider adoption in rechargeable zinc–air batteries. In our opinion, great effort is still needed in the following aspects:

(1) The mechanism of the ORR/OER catalytic process of manganese dioxide-based materials is still not well understood due to the various crystal structures and the complex charge–discharge process. The effect of atom arrangements, phase transition, and oxygen defects on the bifunctional activity still lacks systematic investigation. One typical example is whether there is a lattice oxygen mechanism during the OER process of defective MnO_2. In addition, it is recommended to explore the ORR/OER catalytic process by using *in situ* analytical techniques and measurements, which can provide insights into the catalyst property changes and reaction process in real-time, thus providing more accurate and reliable data, which can help to deeply elucidate the catalyst reaction mechanism and optimise the catalyst design.

(2) The expansion of the surface area of manganese dioxide-based catalysts to improve ORR and OER performance has been studied extensively, but controlling the different exposed crystalline surfaces of manganese dioxide as a cathode in zinc–air batteries has been less studied. Therefore, it is highly demanded that the control of the exposed crystal facets of MnO_2-based catalysts be widely investigated in zinc–air batteries in the future.

(3) In contrast to the single strategy, a combination of multiple strategies is more effective in further improving the activity of MnO_2.

(4) Like in battery science, at the initial stage of the electrochemical catalytic process, the electrochemical reduction of MnO_2 produces unstable Mn^{3+} ions. The Mn^{3+} is considered one of the active sites during the ORR/OER as stated in the manuscript; however, the Mn^{3+} ion undergoes a disproportionation reaction which transforms it into Mn^{2+}, which is highly soluble in the aqueous electrolyte. Subsequently, it migrates to the negative electrode due to the electric field and deposits on the electrode, which has a strong destructive effect on the electrode. The dissolution of Mn^{3+} leads to the loss of active components, which greatly reduces the catalytic stability. Although many efforts have been made to try to solve the manganese dissolution problem, including material doping modification, adjusting the composition of the electrolyte (adding soluble manganese salts, hydrogel electrolyte), *etc.*, manganese dissolution is still a major challenge in the battery field.

Data availability

No primary research results, software or code have been included and no new data were generated or analysed as part of this review.

Conflicts of interest

There are no conflicts to declare.

Acknowledgements

References

1 D. Shindell and C. J. Smith, *Nature*, 2019, **573**, 408–411.

2 Y. Zhang, L. Tao, C. Xie, D. Wang, Y. Zou, R. Chen, Y. Wang, C. Jia and S. Wang, *Adv. Mater.*, 2020, **32**, 1905923.

3 Q. Wang, S. Kaushik, X. Xiao and Q. Xu, *Chem. Soc. Rev.*, 2023, **52**, 6139–6190.

4 Y. Zhang, J. Wang, M. Alfred, P. Lv, F. Huang, Y. Cai, H. Qiao and Q. Wei, *Energy Storage Mater.*, 2022, **51**, 181–211.

5 W. Shang, W. Yu, Y. Liu, R. Li, Y. Dai, C. Cheng, P. Tan and M. Ni, *Energy Storage Mater.*, 2020, **31**, 44–57.

6 F. Yu, L. Pang, X. Wang, E. R. Waclawik, F. Wang, K. Ostrikov and H. Wang, *Energy Storage Mater.*, 2019, **19**, 56–61.

7 C. Feng, M. Lv, J. Shao, H. Wu, W. Zhou, S. Qi, C. Deng, X. Chai, H. Yang, Q. Hu and C. He, *Adv. Mater.*, 2023, **35**, 2305598.

8 G. Notton, M. L. Nivet, C. Voyant, C. Paoli, C. Darras, F. Motte and A. Fouilloy, *Renewable Sustainable Energy Rev.*, 2018, **87**, 96–105.

9 H. Feng, D. Liu, Y. Zhang, X. Shi, O. C. Esan, Q. Li, R. Chen and L. An, *Adv. Energy Mater.*, 2022, **12**, 2200469.

10 R. Wiser, J. Rand, J. Seel, P. Beiter, E. Baker, E. Lantz and P. Gilman, *Nat. Energy*, 2021, **6**, 555–565.

11 W. Sun, F. Wang, B. Zhang, M. Zhang, V. Küpers, X. Ji, C. Theile, P. Bieker, K. Xu, C. Wang and M. Winter, *Science*, 2021, **371**, 46–51.

12 J. Yu, B. Q. Li, C. Zhao and Q. Zhang, *Energy Environ. Sci.*, 2020, **13**, 3253–3268.

13 H. Wang and Q. Xu, *Matter*, 2019, **1**, 565–595.

14 C. Xia, Y. Zhou, C. He, A. I. Douka, W. Guo, K. Qi and B. Xia, *Small Sci.*, 2021, **1**, 2100010.

15 S. Wu, X. Xu, Y. Ren, X. Guo, H. Sun and G. Zhou, *Ionics*, 2022, **28**, 1017–1036.

16 Q. Liu, Z. Pan, E. Wang, L. An and G. Sun, *Energy Storage Mater.*, 2020, **27**, 478–505.

17 G. Nazir, A. Rehman, J. H. Lee, C. H. Kim, J. Gautam, K. Heo, S. Hussain, M. Ikram, A. A. Alobaid, S. Y. Lee and S. J. Park, *Nano-Micro Lett.*, 2024, **16**, 138.

18 Y. Song, W. Li, K. Zhang, C. Han and A. Pan, *Adv. Energy Mater.*, 2024, **14**, 2303352.

19 P. Yu, L. Wang, F. Sun, Y. Xie, X. Liu, J. Ma, X. Wang, C. Tian, J. Li and H. Fu, *Adv. Mater.*, 2019, **31**, 1901666.

20 D. Stock, S. Dongmo, J. Janek and D. Schröder, *ACS Energy Lett.*, 2019, **4**, 1287–1300.

21 S. Ren, X. Duan, S. Liang, M. Zhang and H. Zheng, *J. Mater. Chem. A*, 2020, **8**, 6144–6182.

22 J. Fu, R. Liang, G. Liu, A. Yu, Z. Bai, L. Yang and Z. Chen, *Adv. Mater.*, 2019, **31**, 1805230.

23 X. Lu, Y. Chen, S. Wang, S. Gao and X. Lou, *Adv. Mater.*, 2019, **31**, 1902339.

24 K. Zeng, X. Zheng, C. Li, J. Yan, J. Tian, C. Jin, P. Strasser and R. Yang, *Adv. Funct. Mater.*, 2020, **30**, 2000503.

25 T. Oh, K. Kim and J. Kim, *J. Energy Chem.*, 2019, **38**, 60–67.

26 C. Zhao, J. Liu, J. Wang, D. Ren, B. Li and Q. Zhang, *Chem. Soc. Rev.*, 2021, **50**, 7745–7778.

27 E. Vijayakuma, S. Ramakrishnan, C. Sathiskumar, D. J. Yoo, J. Balamurugan, H. S. Noh, D. Kwon, Y. H. Kim and H. Lee, *Chem. Eng. J.*, 2022, **428**, 131115.

28 Z. Zhou, Y. Liu, J. Zhang, H. Pang and G. Zhu, *Electrochem. Commun.*, 2020, **121**, 106871.

29 S. Yan, Y. Xue, S. Li, G. Shao and Z. Liu, *ACS Appl. Mater. Interfaces*, 2019, **11**, 25870.

30 K. Wu, L. Zhang, Y. Yuan, L. Zhong, Z. Chen, X. Chi, H. Lu, Z. Chen, R. Zou, T. Li, C. Jiang, Y. Chen, X. Peng and J. Lu, *Adv. Mater.*, 2020, **32**, 2002292.

31 M. Varnicic, M. M. Pavlovic, S. E. Pantovic, M. Mihailovic, M. P. R. Pavlovic, S. Stopic and B. Friedrich, *Metals*, 2022, **12**, 22.

32 Y. Guo, Y. Chen, H. Cui and Z. Zhou, *Chin. J. Catal.*, 2019, **40**, 1298–1310.

33 S. Chen, X. Shu, H. Wang and J. Zhang, *J. Mater. Chem. A*, 2019, **7**, 19719–19727.

34 Y. Zhang, Z. Zhang, G. Jiang, A. H. Mamaghani, S. Sy, R. Gao, Y. Jiang, Y. Deng, Z. Bai, L. Yang, A. Yu and Z. Chen, *Nano Energy*, 2022, **100**, 107425.

35 Y. Kumar, M. Mooste and K. Tammeveski, *Curr. Opin. Electrochem.*, 2023, **38**, 101229.

36 X. Han, X. Ling, Y. Wang, T. Ma, C. Zhong, W. Hu and Y. Deng, *Angew. Chem., Int. Ed.*, 2019, **58**, 5359–5364.

37 H. Wang, C. Tang and Q. Zhang, *Adv. Funct. Mater.*, 2018, **28**, 1803329.

38 Z. Li, Q. Wang, X. Bai, M. Wang, Z. Yang, Y. Du, G. E. Sterbinsky, D. Wu, Z. Yang, H. Tian, F. Pan, M. Gu, Y. Liu, Z. Feng and Y. Yang, *Energy Environ. Sci.*, 2021, **14**, 5035–5043.

39 C. Man, H. Su, F. Calle-Vallejo, H. A. Hansen, J. I. Martínez, N. G. Inoglu, J. Kitchin, T. F. Jaramillo, J. K. Norskov and J. Rossmeisl, *ChemCatChem*, 2011, **3**, 1159–1165.

40 M. Busch, N. B. Halck, U. I. Kramm, S. Siahrostami, P. Krtil and J. Rossmeisl, *Nano Energy*, 2016, **29**, 126–135.

41 W. Zhou, H. Su, W. Cheng, Y. Li, J. Jiang, M. Liu, F. Yu, W. Wang, S. Wei and Q. Liu, *Nat. Commun.*, 2022, **13**, 6414.

42 Z. Huang, S. Xi, J. Song, S. Dou, X. Li, Y. Du, C. Diao, Z. Xu and X. Wang, *Nat. Commun.*, 2021, **12**, 3992.

43 Q. Liu, L. Wang and H. Fu, *J. Mater. Chem. A*, 2023, **11**, 4400–4427.

44 F. Xie, H. Li, X. Wang, X. Zhi, D. Chao, K. Davey and S.-Z. Qiao, *Adv. Energy Mater.*, 2021, **11**, 2003419.

45 X. Gao, H. Wu, W. Li, Y. Tian, Y. Zhang, H. Wu, L. Yang, G. Zou, H. Hou and X. Ji, *Small*, 2020, **16**, 1905842.

46 L. Liu, Q. Peng, G. Qiu, J. Zhu, W. Tan, C. Liu, L. Zheng and Z. Dang, *Environ. Pollut.*, 2019, **244**, 783–791.

47 T. Lv, G. Zhang, S. Zheng, X. Guo, T. Chen, S. Yang and H. Pang, *Chem. Eng. J.*, 2022, **440**, 135931.

29380 | *J. Mater. Chem. A*, 2024, **12**, 29355–29382

This journal is © The Royal Society of Chemistry 2024

48 N. L. Okamoto, H. Yoshisako and T. Ichitsubo, *Energy Storage Mater.*, 2023, **61**, 102912.

49 Y. Zhao, P. Zhang, J. Liang, X. Xia, L. Ren, L. Song, W. Liu and X. Sun, *Energy Storage Mater.*, 2022, **47**, 424–433.

50 L. Shan, Y. Zhang, Y. Xu, M. Gao, T. Xu and C. Si, *Adv. Compos. Hybrid Mater.*, 2023, **6**, 174.

51 H. Luo, B. Zhang, H. Zhang, Q. Zheng, X. Wu, Y. Yan, Z. Li, Y. Tang, W. Hao, G. Liu, Y. Hong, J. Ye, Y. Qiao and S. Sun, *J. Phys. Chem. Lett.*, 2023, **14**, 4565–4574.

52 Z. Ma, J. Li and T. Ling, *Trans. Tianjin Univ.*, **28**, 193–198.

53 V. S. Kumbhar, H. Lee, J. Lee and K. Lee, *Carbon Resour. Convers.*, 2019, **2**, 242–255.

54 Y. Dong, J. Zhao, J. Zhang, Y. Chen, X. Yang, W. Song, L. Wei and W. Li, *Chem. Eng. J.*, 2020, **388**, 124244.

55 L. Miao, J. Wang and P. Zhang, *Appl. Surf. Sci.*, 2019, **466**, 441–453.

56 X. Liu, J. Yi, K. Wu, Y. Jiang, Y. Liu, B. Zhao, W. Li and J. Zhang, *Nanotechnology*, 2020, **31**, 122001.

57 E. Davari and D. G. Ivey, *Sustainable Energy Fuels*, 2018, **2**, 39–67.

58 B. Chen, H. Miao, R. Hu, M. Yin, X. Wu, S. Sun, Q. Wang, S. Li and J. Yuan, *J. Alloys Compd.*, 2021, **852**, 157012.

59 J. Yang, J. Wang, S. Ma, B. Ke, L. Yu, W. Zeng, Y. Li and J. Wang, *Phys. E*, 2019, **109**, 191–197.

60 T. Subramaniam, M. B. Idris, G. H. Sai and S. Devaraj, *Mater. Chem. Phys.*, 2023, **303**, 127845.

61 P. K. Gupta, A. Bhandari, S. Saha, J. Bhattacharya and R. G. S. Pala, *J. Phys. Chem. C*, 2019, **123**, 22345–22357.

62 Y. Gu, G. Yan, Y. Lian, P. Qi, Q. Mu, C. Zhang, Z. Deng and Y. Peng, *Energy Storage Mater.*, 2019, **23**, 252–260.

63 R. K. Mathur and A. Halder, *Catal. Sci. Technol.*, 2020, **10**, 7352–7364.

64 Z. Zhou, X. Zheng, M. Liu, P. Liu, S. Han, Y. Chen, B. Lan, M. Sun and L. Yu, *Chemsuschem*, 2022, **15**, e202200612.

65 Y. Li, X. Li, H. Duan, S. Xie, R. Dai, J. Rong, F. Kang and L. Dong, *Chem. Eng. J.*, 2022, **441**, 136008.

66 S. Rong, P. Zhang, F. Liu and Y. Yang, *ACS Catal.*, 2018, **8**, 3435–3446.

67 D. W. Kim, C. Senthil, S. M. Jung, S. S. Kim, H. S. Kim, J. W. Hong, J. H. Ahn and H. Y. Jung, *Energy Storage Mater.*, 2022, **47**, 472–481.

68 L. Liu, Y. Wu, L. Huang, K. Liu, B. Duployer, P. Rozier, P. L. Taberna and P. Simon, *Adv. Energy Mater.*, 2021, **11**, 2101287.

69 K. Chu, Y. Liu, Y. Li, Y. Guo, Y. Tian and H. Zhang, *Appl. Catal., B*, 2020, **264**, 118525.

70 C. Shao, K. Yin, F. Liao, W. Zhu, H. Shi and M. Shao, *J. Alloys Compd.*, 2021, **860**, 158427.

71 G. Cheng, P. Liu, S. Chen, Y. Wu, L. Huang, M. Chen, C. Hu, B. Lan, X. Su, M. Sun and L. Yu, *Colloids Surf.*, 2022, **637**, 128228.

72 Y. Zhou, F. Chen, R. Tian, S. Huang, R. Chen, M. Li, T. Wan, Z. Han, D. Wang and D. Chu, *Surf. Interfaces*, 2021, **26**, 101398.

73 Y. Chen, S. Yang, H. Liu, W. Zhang and R. Cao, *Chin. J. Catal.*, 2021, **42**, 1724–1731.

74 S. Song, W. Li, Y. Ruan, X. Qin, D. Zhang and Y. Xu, *J. Alloys Compd.*, 2020, **834**, 155090.

75 B. Lan, H. Zhong, J. Cao, H. Chen, Z. Zhou, L. Zhang, J. Duan, M. Sun and L. Yu, *Inorg. Chem. Commun.*, 2022, **146**, 110143.

76 R. K. Mathur and A. Halder, *Mater. Today Energy*, 2021, **19**, 100612.

77 A. Chowdhury, K. C. Lee, M. S. W. Lim, K. Pan, J. Chen, S. Chong, C. Huang, G. Pan and T. Yang, *Processes*, 2021, **9**, 1087.

78 J. Xu, Q. Gao, Y. Xia, X. Lin, W. Liu, M. Ren, F. Kong, S. Wang and C. Lin, *J. Colloid Interface Sci.*, 2021, **598**, 419–429.

79 J. Xu, X. Hu, M. A. Alam, G. Muhammad, Y. Lv, M. Wang, C. Zhu and W. Xiong, *RSC Adv.*, 2021, **11**, 35280–35286.

80 S. Ni, H. Zhang, Y. Zhao, X. Li, Y. Sun, J. Qian, Q. Xu, P. Gao, D. Wu, K. Kato, M. Yamauchi and Y. Sun, *Chem. Eng. J.*, 2019, **366**, 631–638.

81 Q. Hu, S. Qi, Q. Huo, Y. Zhao, J. Sun, X. Chen, M. Lv, W. Zhou, C. Feng, X. Chai, H. Yang and C. He, *J. Am. Chem. Soc.*, 2024, **146**, 2967–2976.

82 H. Kim, K. Min, S. E. Shim, D. Lim and S. H. Baeck, *Int. J. Hydrogen Energy*, 2022, **47**, 2378–2388.

83 K. Ma, Q. Li, C. Hong, G. Yang and C. Wang, *ACS Appl. Mater. Interfaces*, 2021, **13**, 55208–55217.

84 T. He, X. Zeng and S. Rong, *J. Mater. Chem. A*, 2020, **8**, 8383–8396.

85 J. Zhou, X. He, Z. Zhou and F. Li, *J. Solid State Electrochem.*, 2022, **26**, 335–341.

86 X. Jin, M. He, F. Chen, K. Li, J. Min, Z. Wang and J. Li, *Chem. Eng. J.*, 2023, **464**, 142712.

87 G. M. S. Salvador, A. L. Silva, L. P. C. Silva, F. B. Passos and N. M. F. Carvalho, *Int. J. Hydrogen Energy*, 2021, **46**, 26976–26988.

88 Y. Zhao, J. Zhang, W. Wu, X. Guo, P. Xiong, H. Liu and G. Wang, *Nano Energy*, 2018, **54**, 129–137.

89 H. Zhang, Y. Jia, Y. Li, L. Wang, C. Ouyang and S. Zhong, *Int. J. Hydrogen Energy*, 2023, **48**, 2652–2662.

90 S. Ni, H. Zhang, Y. Zhao, X. Li, Y. Sun, J. Qian, Q. Xu, P. Gao, D. Wu, K. Kato, M. Yamauchi and Y. Sun, *Chem. Eng. J.*, 2019, **366**, 631–638.

91 W. Xiang, Y. Zhao, Z. Jiang, X. Li, H. Zhang, Y. Sun, Z. Ning, F. Du, P. Gao, J. Qian, K. Kato, M. Yamauchi and Y. Sun, *J. Mater. Chem. A*, 2018, **6**, 23366–23377.

92 N. V. Bôas, J. B. Souza, L. C. Varanda, S. A. S. Machado and M. L. Calegaro, *Appl. Catal., B*, 2019, **258**, 118014.

93 S. K. Mathur, A. Singh, R. Mitra, R. Sharma, K. Biswas and A. Halder, *J. Energy Storage*, 2023, **74**, 109350.

94 W. Zhang, S. Xie, S. Wang, P. Zhao, X. Yang, P. Huang, P. Liu and F. Cheng, *Chem. –Eur. J.*, 2023, **29**, e202203787.

95 Z. Huang, J. Song, S. Dou, X. Li, J. Wang and X. Wang, *Matter*, 2019, **1**, 1494–1518.

96 Y. Gu, Y. Min, L. Li, Y. Lian, H. Sun, D. Wang, M. H. Rummeli, J. Guo, J. Zhong, L. Xu, Y. Peng and Z. Deng, *Chem. Mater.*, 2021, **33**, 4135–4145.

97 W. Chen, Z. Liu, Y. Li, Q. Liao and X. Zhu, *Energy*, 2021, **222**, 119971.

This journal is © The Royal Society of Chemistry 2024

J. Mater. Chem. A, 2024, **12**, 29355–29382 | 29381

98 Y. Munaiah, S. Boopathi, S. S. Kumar and P. Ragupathy, *Mater. Lett.*, 2019, **239**, 184–191.

99 Z. Huang, G. Li, Y. Huang, X. Gu, N. Wang, J. Liu, O. Li, H. Shao, Y. Yang and Z. Shi, *J. Power Sources*, 2020, **448**, 227385.

100 P. Xu, Q. Gan, L. Ma, Z. Li, H. Zhang, H. Xiao, X. Liang, T. Zhang, X. Tian and C. Liu, *Carbon*, 2019, **149**, 452–461.

101 X. Yang, W. Peng, K. Fu, L. Mao, J. Jin, S. Yang and G. Li, *Electrochim. Acta*, 2020, **340**, 135989.

102 Z. Tong, Y. Yuan, S. Yin, B. Wang, M. Zhu and S. Guo, *Sustainable Mater. Technol.*, 2021, **29**, e00312.

103 G. Elmaci, A. S. Ertürk, M. Sevim and Ö. Metin, *Int. J. Hydrogen Energy*, 2019, **44**, 17995–18006.

104 S. He, K. Xiao, X. Chen, T. Li, T. Ouyang, Z. Wang, M. Guo and Z. Liu, *J. Colloid Interface Sci.*, 2019, **557**, 644–654.

105 M. A. Marsudi, Y. Ma, B. Prakoso, J. J. Hutani, A. Wibowo, Y. Zong, Z. Liu and A. Sumboja, *Catalysts*, 2020, **10**, 64.

106 X. Zhang and L. Wang, *J. Power Sources*, 2021, **507**, 230280.

107 L. Tian, J. Wang, K. Wang, H. Wo, X. Wang, W. Zhuang, T. Li and X. Du, *Carbon*, 2019, **143**, 457–466.

108 G. Dong, B. Sun, T. Su, L. Hao, D. Chai, W. Zhang, Z. Zhang, M. Zhao and J. Li, *J. Electrochem. Soc.*, 2022, **169**, 054508.

109 N. Xu, Q. Nie, L. Luo, C. Yao, Q. Gong, Y. Liu, X. Zhou and J. Qiao, *ACS Appl. Mater. Interfaces*, 2019, **11**, 578–587.

110 H. Miao, B. Chen, S. Li, X. Wu, Q. Wang, C. Zhang, Z. Sun and H. Li, *J. Power Sources*, 2020, **450**, 227653.

111 X. Xiao, W. Zhang, H. Zhao, L. Li, P. Deng, Y. Wu, S. Luo and B. Chen, *Ceram. Int.*, 2022, **48**, 6506–6511.

112 D. Yang, Z. Li, M. Liu, X. Zhang, Y. Chen, H. Xue, E. Ye and R. Luque, *ACS Sustain. Chem. Eng.*, 2019, **7**, 4564–4585.

113 Q. Hu, K. Gao, X. Wang, H. Zheng, J. Cao, L. Mi, Q. Huo, H. Yang, J. Liu and C. He, *Nat. Commun.*, 2022, **13**, 3958.

114 J. Qu, S. Lv, X. Peng, S. Tian, J. Wang and F. Gao, *J. Alloys Compd.*, 2016, **671**, 17–23.

115 X. Xiao, X. Hu, Y. Liang, G. Zhang, X. Wang, Y. Yan, X. Li, G. Yan and J. Wang, *J. Power Sources*, 2020, **476**, 228684.

116 J. Chen, H. Li, C. Fan, Q. Meng, Y. Tang, X. Qiu, G. Fu and T. Ma, *Adv. Mater.*, 2020, **32**, 2003134.

117 S. Song, W. Li, Y. Deng, Y. Ruan, Y. Zhang, X. Qin and Z. Chen, *Nano Energy*, 2020, **67**, 104208.

118 M. Han, M. Shi, J. Wang, M. Zhang, C. Yan, J. Jiang, S. Guo, Z. Sun and Z. Guo, *Carbon*, 2019, **153**, 575–584.

119 Y. Wang, F. Wang, Y. Fang, J. Zhu, H. Luo, J. Qi and W. Wu, *Appl. Surf. Sci.*, 2019, **496**, 143566.

120 R. Zhang, L. Huang, Z. Yu, R. Jiang, Y. Hou, L. Sun, B. Zhang, Y. Huang, B. Ye and Y. Zhang, *Electrochim. Acta*, 2019, **323**, 134845.

121 L. Wang, D. Kong, F. Chen, L. Cui, Y. Cai, H. Wang, X. Zhong, Y. Huang, Q. Li, Z. Ma and S. Hu, *Energy Fuels*, 2021, **35**, 16829–16836.

122 K. Worku, D. W. Ayele, N. G. Habtu and T. A. Yemata, *Heliyon*, 2021, **7**, e08076.

123 B. Liu, Y. Zhang, J. Wang, J. Wang, Z. Su, G. Li and T. Jiang, *Adv. Powder Technol.*, 2019, **30**, 302–310.

124 B. Yu, R. Xu, B. Chen, X. Wang and S. He, *Int. J. Hydrogen Energy*, 2023, **48**, 11131–11140.

125 N. Xu, J. Qiao, X. Zhang, C. Ma, S. Jian, Y. Liu and P. Pei, *Appl. Energy*, 2016, **175**, 495–504.

126 Y. Wang, J. Liu, H. Yuan, F. Liu, T. Hu and B. Yang, *Adv. Funct. Mater.*, 2023, **33**, 2211909.

127 J. Yang, J. Wang, L. Zhu, W. Zeng and J. Wang, *Mater. Lett.*, 2019, **234**, 331–334.

128 J. Xu, P. Gu, D. J. S. Birch and Y. Chen, *Adv. Funct. Mater.*, 2018, **28**, 1801573.

129 N. Alwadai, S. Manzoor, M. Al Huwayz, M. Abdullah, R. Y. Khosa, S. Aman, A. G. Abid, Z. A. Alrowaili, M. S. Al-Buriahi and H. M. T. Farid, *Surf. Interfaces*, 2023, **36**, 102467.

130 P. Wang, Y. Lin, L. Wan and B. Wang, *ACS Appl. Mater. Interfaces*, 2019, **11**, 37701–37707.

131 J. H. Hong, J. H. Kim, G. D. Park, J. Y. Lee, J. K. Lee and Y. C. Kang, *Chem. Eng. J.*, 2021, **414**, 128815.

132 N. Xu, Y. Zhang, Y. Wang, M. Wang, T. Su, C. A. Coco, J. Qiao and X. Zhou, *Appl. Energy*, 2020, **279**, 115876.

133 Q. Hu, W. Zhou, S. Qi, Q. Huo, X. Li, M. Lv, X. Chen, C. Feng, J. Yu, X. Chai, H. Yang and C. He, *Nat. Sustain.*, 2024, **7**, 442–451.

134 J. Jia, L. Lei, X. Lian, F. Zheng, L. Song, G. Hu and H. Niu, *Nanoscale*, 2021, **13**, 11120–11127.

135 F. Cheng, T. Zhang, Y. Zhang, J. Du, X. Han and J. Chen, *Angew. Chem., Int. Ed.*, 2013, **52**, 2474–2477.

136 S. Lee, G. Nam, J. Sun, J.-S. Lee, H.-W. Lee, W. Chen, J. Cho and Y. Cui, *Angew. Chem., Int. Ed.*, 2016, **55**, 8599–8604.

137 Y. Choi, D. Lim, E. Oh, C. Lim and S. H. Baeck, *J. Mater. Chem. A*, 2019, **7**, 11659–11664.

138 Y. Zhong, J. Dai, X. Xu, C. Su and Z. Shao, *ChemElectroChem*, 2020, **7**, 4949–4955.

29382 | *J. Mater. Chem. A*, 2024, **12**, 29355–29382

This journal is © The Royal Society of Chemistry 2024